The Thesis Committee for Sarah E. Muschinske Certifies that this is the approved version of the following thesis:

Transport Behavior and Weak Adhesion of Quantum Confined Epitaxial Bi and $Bi_{1-x}Sb_x$ Films

APPROVED BY
SUPERVISING COMMITTEE:

Professor Seth R. Bank, Supervisor

Professor Deji Akinwande

Transport Behavior and Weak Adhesion of Quantum Confined Epitaxial Bi and $Bi_{1-x}Sb_x$ Films

by

Sarah E. Muschinske

Thesis

Presented to the Faculty of the Graduate School of

The University of Texas at Austin

in Partial Fulfillment

of the Requirements

for the Degree of

Master of Science in Engineering

The University of Texas at Austin

May 2018

Acknowledgements

I would like to thank my advisor, Professor Seth Bank, for his limitless advice and support throughout both my bachelor's and master's degrees. I would also like to profusely thank Dr. Emily Walker for her guidance and mentorship. I would not be here if not for her help and the bismuth she has grown.

In addition, I would like to thank Professor Deji Akinwande for his advice and for the valuable lessons and skills I learned working in his research group as an undergraduate. I would like to thank our collaborators Professor Kenneth Leichti, Professor Minjoo L. Lee, Professor Sayeef Salahuddin, Dr. Seung Ryul Na, Tianhao Yang, Yukun Sun, and Niklas Roschewsky for all the time and effort they put into this project. I would like to thank Professor Delia Milliron and Corey Staller for training me on, and allowing me to use their lab equipment. Finally, I would like to thank all of the amazing people in our group who contributed to the acquisition of the measurements presented in this thesis including Stephen March, Andrew Briggs, Susan Tan, and Alice Yau.

Abstract

Transport Behavior and Weak Adhesion of Quantum Confined Epitaxial Bi and $Bi_{1-x}Sb_x$ Films

Sarah E/ Muschinske, MSE

The University of Texas at Austin, 2018

Supervisor: Seth R. Bank

Novel devices, such as those based on principles of spin and magnetization instead of traditional electronic transport, necessitate the development of new materials systems. Bismuth (Bi) is a promising materials systems for these applications due to its high mobility, large spin-orbit interaction and metallic surface states which exhibit Rashba spin-splitting. In addition, Bi exhibits a thickness dependent band gap due to quantum size effects occurring at uniquely long length scales (>100nm) due to its large de Broglie wavelength. This allows the metallic surface states to be isolated from the bulk in the band gap. Alloying Bi with antimony (Sb) to create $Bi_{1-x}Sb_x$ allows access to topologically non-trivial surface states which have the aforementioned qualities associated with Bi, as well as added protection against backscattering and non-magnetic perturbation. In addition, the non-trivial topology of $Bi_{1-x}Sb_x$ makes it a contender for topological quantum computing devices using Majorana fermions and braided states.

In this thesis, we explore the transport properties of Bi and $Bi_{1-x}Sb_x$ as the film thicknesses and alloy compositions are varied, providing a basis for custom design of these

materials for specific applications. In addition, we report advances in the understanding of Bi and $Bi_{1-x}Sb_x$ growth on Si (111) through the measurement of their weak adhesion to the Si (111) substrate as well as the identification of (012) oriented crystal growth of $Bi_{1-x}Sb_x$ and the effect of this crystal structure transition on the transport properties of the films. Finally, we report the development of a dry transfer method which can be used to transfer high quality epitaxial Bi and $Bi_{1-x}Sb_x$ films to arbitrary substrates which may facilitate their integration into novel spin-based devices.

Table of Contents

List of Tables

List of Figures

Chapter 1: Introduction

Scaling limitations of conventional CMOS devices motivate the exploration of novel logic-device paradigms such as those based on spintronics and quantum information [1]–[3]. Bi and $Bi_{1-x}Sb_x$ have great potential for these applications due to their metallic surface states. These surface states are trivial and Rashba spin-split in Bi and topologically non-trivial and spin-momentum locked in $Bi_{1-x}Sb_x$[4], [5]. These materials are strong contenders for production of spin-polarized currents because of their large spin-orbit interactions and because the spin-dependent properties of their surface states provide protection against spin-independent scattering events. Additionally, high quality epitaxial Bi and $Bi_{1-x}Sb_x$ are good candidates for spintronic integration in standard CMOS technologies due to their ability to be grown on Si[6].

1.1 SPINTRONIC DEVICES

Spintronic devices are logic devices that switch between two states of electron spin or material magnetization instead of voltage[1]. The most mature of spintronic technologies is found in magnetic memory. These technologies use switching mechanisms such as spin transfer torque (STT) and spin orbit torque (SOT) allow all-electrical control over magnetic polarization in the recording layer of the memory device[7]. Both of these processes have the potential to be made much lower power than conventional magnetic memory which uses current-induced magnetic fields for switching. STT works by injecting a spin polarized current into a ferromagnetic (FM) recording layer which transfers angular momentum to the FM and switches its magnetization[8], [9]. Unfortunately, STT devices currently require too high of current to be tractable for commercial application. This is primarily because the spin-polarized current is created by passing a current through a thick

magnetic layer which filters it by spin. This strong limits the amount of spin current that can be created by a given charge current. SOT is a similar effect, but requires a pure spin current to induce a spin torque which transfers angular momentum to a FM memory layer without injection[10].

To utilize SOT, all electrical generation of pure spin current must be achieved. This has been demonstrated through the use of the spin hall effect (SHE)[11]. The SHE is phenomenon seen in materials with large spin-orbit interaction, through which a charge current can be converted to a spin current by means of spin-dependent scattering without the application of a magnetic field[12]. A similar phenomena known as the inverse spin Hall effect (ISHE) results in the conversion of a spin current to a charge current. Topological insulators are considered very appealing for spintronic devices due to their ability to create strongly spin-polarized currents as well as their protection against backscattering[13]. Studies on the use of topological insulators for producing spin currents have thus far shown great success[14], [15].

1.2 TOPOLOGICAL INSULATORS

Topology is a concept borrowed from the field of mathematics which defines shapes by their ability to be continuously deformed into one another[16]. The analogue to this in solid-state physics is the ability to adiabatically transition between the band structures of two different insulators. The idea of defining a material system by its topological order was introduced as a way of explaining the quantum Hall state in the 1980's [17]. The quantum hall state is defined by a quantized Hall conductivity that is robust to smooth changes to the material properties. The quantum Hall effect creates chiral 1D edge states where electrons can only propagate in one direction in a "skipping"-style half cyclotron orbit along each edge of the material. However, as the source of the quantum

Hall phase, the Hall conductivity, is odd under time reversal, the quantum Hall phase can only exist in states with broken time reversal symmetry such as systems under strong external magnetic field.

The 2D quantum spin Hall (QSH) insulator was first theorized in 2006 as an extension of the quantum Hall effect with the additional consideration of spin-orbit coupling which allows for two opposite electron paths along each edge of the material with similarly opposite spins[18], [19]. As the QSH insulator has "helical" counterpropagating states on each edge, it is invariant under time reversal and thus does not necessitate the presence of a magnetic field. Stacking of 2D topological insulators can form weak 3D topological insulators which are analogous to the quantum spin Hall phase, but, like with the quantum Hall states, this topological behavior can only occur in systems where time reversal symmetry is broken[20], [21]. Conversely, strong 3D topologically insulating behavior is dependent only on time-reversal symmetry being maintained and thus is robust to all non-magnetic perturbation[20], [22]. 3D topological insulators are defined by an invariant which requires there be an odd number of Dirac points within the Fermi surface. As time reversal symmetry must be maintained in a 3D topological insulator, electrons at opposite points in momentum space must also have opposite spins, i.e. the spin and momentum are "locked". Due to the odd number of Dirac points, an electron circling the Fermi surface will experience a spin rotation of 2π resulting in a π-Berry phase. The π-Berry phase forces electrons on reversed paths to interact destructively which protects against both localization and backscattering .

The appealing proposed properties of topological insulators such as their robustness to spin-independent scattering and localization made their experimental realization a matter of great interest as they could promise near-lossless transport. In 2007, the first 2D topological insulator was experimentally realized as a HgTe quantum well [23]. Only a

year later, $Bi_{1-x}Sb_x$ was the first experimentally determined 3D topological insulator in 2008[5]. In both materials, the p-orbital band is pushed above the s-orbital band due to the very strong spin-orbit coupling. The resulting band inversion causes an inversion of symmetry which results in a topologically non-trivial state [24].

The topological nature of these films makes them appealing for spin-based devices due to the combination of large spin-orbit interaction, spin-momentum locked channels, and symmetry protections against backscattering. In addition, topological insulators are very appealing for the exploration of novel physics such as Majorana fermions and mirror magnetic monopoles[25].

1.3 MOTIVATION FOR THIS WORK

Our candidate topological insulator, $Bi_{1-x}Sb_x$, has been somewhat less popular for study compared to bismuth chalcogenides (such as binary Bi_2X_3, ternary $Bi_2X_xY_{3-x}$, and quaternary ($Bi_{2-x}Sb_xX_{3-y}Y_y$, where X and Y are chalcogens such as S, Se, or Te). This is primarily due to $Bi_{1-x}Sb_x$'s comparatively more complex and limiting growth process as well as its small bandgap (~30 meV)[26]. Bismuth chalcogenides are van der Waals materials which form in sheets of quintuple layers and thus can be easily fabricated on arbitrary substrates with van der Waals epitaxy or through bulk exfoliation[27]. In addition, the larger bandgaps of bismuth chalcogenides (100-400 meV) allows for easier isolation of the surface states[28], [29]. While these properties make bismuth chalcogenides very appealing for physical studies of topological phases, $Bi_{1-x}Sb_x$ has some unique advantages for device applications. Notably, $Bi_{1-x}Sb_x$ has a much higher conductivity than bismuth chalcogenides that is more similar the magnitude of conductivity present in most FMs[30]. This would allow significant reduction in the loss of SHE-based devices as much less

current will be shunted through the FM layer – paving the way towards ultra-low-power spintronics.

The limitation of conductivity matching FM materials makes exploration of other materials with large spin-orbit interactions a useful pursuit. Our other candidate material, Bi, is a semimetal in its bulk form but quantum confinement induces a small bandgap in films thinner than ~100 nm[31]. In addition, the Rashba effect causes spin-split surface states to form in the bandgap[32]. The combination of these spin-split surface states, large bulk conductivity, and large spin-orbit interaction indicates Bi has great potential for spin current generation[33].

In this thesis, we work towards realization of devices based on Bi and $Bi_{1-x}Sb_x$'s unique properties through greater understanding of their transport and through process development to facilitate integration into CMOS devices.

Chapter 2: Material Growth and Structural Characterization

In this chapter, we provide an overview of the unique material properties of both Bi and $Bi_{1-x}Sb_x$ as well as our work to grow and characterize these materials. We provide background on the well-known growth modes of Bi on Si (111) and the yet unascertained growth modes of $Bi_{1-x}Sb_x$ on the same substrate. We give a brief overview of the growth method used to produce our highly crystalline films as well as a demonstration of the crystalline orientation and quality. We find that $Bi_{1-x}Sb_x$ exhibits a composition-dependent crystalline orientation in very thin films which has been previously unobserved. Finally, we discuss the incorporation of Sb into $Bi_{1-x}Sb_x$ alloys, the associated growth parameters for targeted film compositions, and oxidation effects on the composition.

2.1 MATERIALS BACKGROUND

Although Bi and $Bi_{1-x}Sb_x$ have been studied in the bulk form since the 1960's, there is significantly less known about their form in films thinner than 100 nm where the films are expected to exhibit quantum confinement effects. The interest in these materials primarily stems from their extreme properties including a very high thermoelectric figure of merit and large spin-orbit interaction – making them a very appealing testbed for basic research of unique thermal and spin-orbit phenomena.

2.1.1 Properties of Bi

In its bulk form, Bi is a semimetal with a very small (~38 meV) overlap of the L-point conduction band and the T-point valence band. Bulk Bi has many unique properties stemming from its long de Broglie wavelength, high mobility, large spin-orbit interaction, and large thermoelectric figure of merit[34], [35]. The long de Broglie wavelength seen in Bi results in thin films experiencing quantum size effects at uniquely long length scales on

the order of 200 nm. These quantum size effects have been demonstrated, using angle-resolve photoemission spectroscopy (ARPES), to push the valence and conduction bands apart resulting in an indirect band gap in thin films less than a critical thickness around 100 nm[36]. In addition, the strong spin-orbit coupling combined with broken inversion symmetry at the surface of Bi films results in the Rashba effect causing spin splitting in the surface bands that has also been observed using spin-resolved ARPES[4]. In all of these films, a significant amount of the transport behavior has been attributed to surface states[32]. In addition, previous studies have observed the shifting of the Fermi level in very thin films as well as hybridization between the bulk and surface bands[33], [37]. The combination of quantum confined semiconducting bulk states and metallic surface states makes the electronic properties of Bi thin films highly dependent on film thickness. Although the films' surface states are thought to be topologically trivial, the spin-split nature of the surface states still makes Bi an interesting material for applications in spintronics.

Growth of high quality epitaxial Bi films using molecular beam epitaxy has been demonstrated on Si (111) [6], [38]. This growth is possible due to the commensurate lattice matching of every 6^{th} Bi atom to every 7^{th} Si atom, resulting in coherent strain despite the large difference (15%) between the lattice constants of the two materials[39]. The growth of these films has been demonstrated with *in situ* studies to occur in three distinct phases[40], [41]. In the initial growth phase, the first monolayer of Bi forms a disordered wetting layer on the Si (111) substrate. After this initial layer, growth proceeds in an A17 puckered layer structure analogous to that of black phosphorus. This growth mode continues for the next approximately 4-7 nm of growth before an allotropic transformation occurs and Bi begins growing in its bulk rhombohedral A7 structure. The unique

characteristics of this growth process results in the Bi films exhibiting unexpectedly low interaction with the substrate[42].

2.1.2 Properties of $Bi_{1-x}Sb_x$

$Bi_{1-x}Sb_x$ exhibits similar properties to Bi including high thermoelectric figure of merit, high room temperature mobility, and large spin-orbit interaction[43], [44]. Additionally, $Bi_{1-x}Sb_x$ was the first experimentally verified 3D topological insulator[45]. Topologically insulating $Bi_{1-x}Sb_x$ is characterized by two surface bands which exhibit 5 distinct Dirac points within the Fermi surface. $Bi_{1-x}Sb_x$ exhibits composition-dependent band structure which allows the band structure to be tuned between semimetallic and semiconducting behavior[46]. The known topologically insulating composition range of the $Bi_{1-x}Sb_x$ alloy is 7-22% Sb, outside of which $Bi_{1-x}Sb_x$ is anticipated to exhibit trivial spin-split surface states similar to those found in pure Bi[47]. This makes $Bi_{1-x}Sb_x$ an ideal material for studies of spin transport in topologically trivial and topologically non-trivial systems.

We can observe the dependence of the high symmetry points in the bulk $Bi_{1-x}Sb_x$ band structure on Sb composition in Figure 2.1. The 0% Sb point shows the symmetry points as they are present in pure semimetallic bulk Bi. As the Sb composition is increased, the conduction band minima at the T-point is observed to decrease and the valence band maxima at the L-point is seen to increase. These points cross, resulting an indirect bandgap semiconducting phase, in Sb compositions from 7-9% [48]. The conduction band present at the L-point also increases with Sb composition resulting in a band inversion in compositions higher than 4% Sb which results in a topologically insulating phase from 7-22% Sb composition.

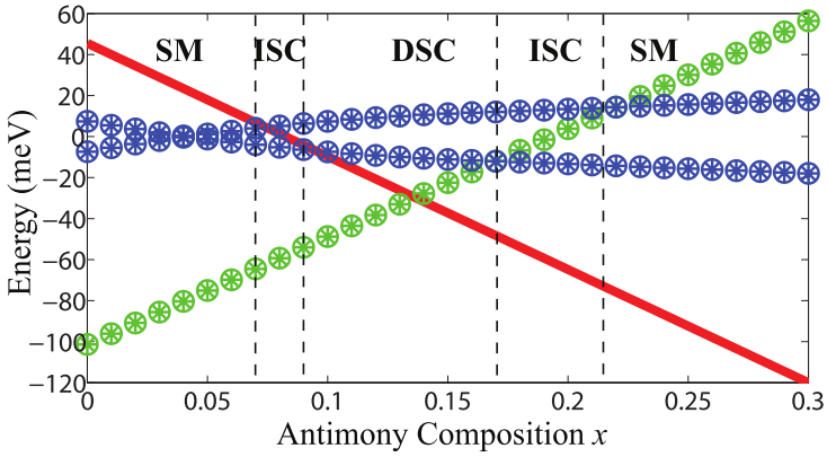

Figure 2.1: Theoretical band structure of $Bi_{1-x}Sb_x$ from Tang et al. with the high symmetry points evaluated as a function of Sb composition[48]. The T-point is shown in red, the 3 degenerate L-points are shown in blue, and the 6 degenerate H-points are shown in green.

As the Sb concentration increases further, the T point is further reduced in energy, eventually decreasing past the L-point valence band and resulting in a direct gap semiconducting phase from 9-17% Sb. In films of compositions from 17-22% Sb, the H-point conduction band is pushed above the L-point conduction band, resulting in an indirect gap between the H-point minima and L-point maxima. Films with higher than 22% composition of Sb are semimetallic with overlapping L and H bands as seen in pure Sb[26].

Quantum confinement effects are expected to influence the band structure of $Bi_{1-x}Sb_x$ at similar length scales to those seen in Bi. This will allow another degree of tunability in $Bi_{1-x}Sb_x$'s band structure and is predicted to create a larger bandgap in the topologically insulating phase which will allow easier isolation of the surface states[46]. ARPES measurements of <24 nm epitaxial films of $Bi_{1-x}Sb_x$ have demonstrated that the films exhibit topologically nontrivial metallic surface states and an insulating bulk in compositions from 8-16% Sb[49]. This is good indication that the formation of the

topologically insulating phase can be achieved in the quantum confinement thickness regime.

Thin films of $Bi_{1-x}Sb_x$ have been significantly less studied than bulk crystals, although they can be grown on a variety of substrates with MBE[50]–[52]. Like Bi, $Bi_{1-x}Sb_x$ can be grown in an A7 rhombohedral structure on Si (111)[49]. To our knowledge, extensive *in situ* analysis of the growth modes of $Bi_{1-x}Sb_x$ has not previously been performed, although a similar transition in the reflection high energy diffraction (RHEED) pattern is seen around 4 nm of growth which in Bi is correlated with the transition from the A17 puckered layer allotrope to the bulk rhombohedral A7 allotrope. This indicates that $Bi_{1-x}Sb_x$ may form a similar puckered layer allotrope during the early stages of growth.

2.2 GROWTH AND CHARACTERIZATION

All films studied in this thesis are grown using molecular beam epitaxy (MBE) in a Varian Gen II MBE system. MBE growth allows very precise manipulation of film thickness and composition as films can be grown through planar stacking of single atomic layers. This method is necessary for the growth of highly crystalline Bi. Other methods used to fabricate Bi thin films such as sputtering and e-beam evaporation typically result in polycrystalline material with grain boundaries leading to reduced mobility. All Bi films are grown at room temperature at growth rates varying between 0.03 – 0.2 Å/s. A higher growth rate of approximately 0.5 Å/s was found to be necessary for the $Bi_{1-x}Sb_x$ films to achieve fluxes high enough to create alloys with the intended low Sb percentages. All films are grown on high resistivity (3500 Ω-cm to intrinsic) Si (111) substrates. The growth rates for the films were calibrated using x-ray reflectivity (XRR). Greater detail about the growth process and calibration can be found in the PhD dissertation by E.S. Walker [53].

2.2.1 Crystalline Orientation

We analyze the crystalline quality and orientation of our films using X-ray diffraction (XRD) measurements. XRD uses a beam of X-rays to strike a material. The atomic layers of the material scattering the beam, producing a diffraction pattern which can be analyzed to identify the crystalline orientations present in the film. The $\omega - 2\theta$ values of all XRD measurements reported in this thesis are aligned to the Si (111) substrate peak.

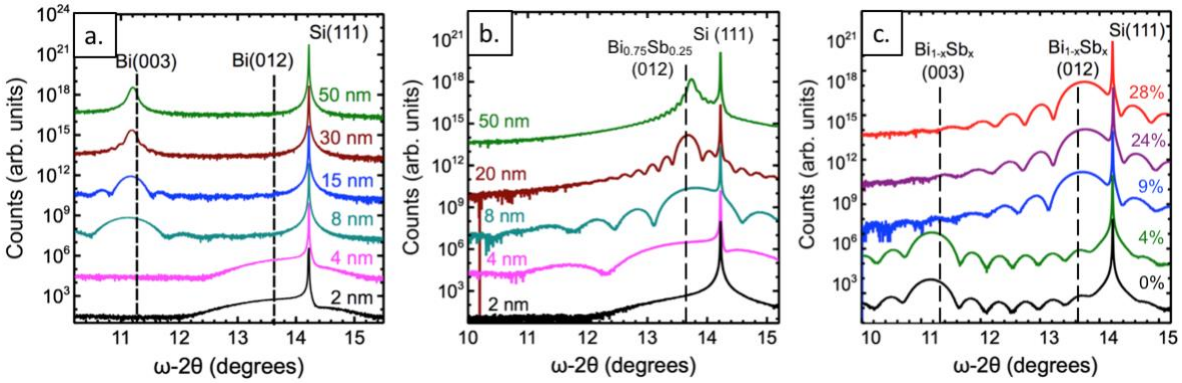

Figure 2.2: XRD of a.) Bi and b.) $Bi_{0.75}Sb_{0.25}$ at various film thicknesses and c.) $Bi_{1-x}Sb_x$ at various compositions

The XRD measurements in Figure 2.2 show that our epitaxially grown Bi and $Bi_{1-x}Sb_x$ films are oriented in the (001) and (012) directions with no anomalous phases[1]. The well-defined interference fringes seen in both materials indicate that the films are highly crystalline. The change in structure of the Bi film from the (001) to the (012) orientation between 4 nm and 8 nm aligns with the previously observed transition in Bi from the puckered layer phase (A17 structure) to its bulk rhombohedral form (A7 structure)[54]. This structural transition is expected to correlate with a significant change in the electrical

[1] We would like to note that notation use throughout this document to refer to the crystalline orientation is with regard to the hexagonal unit cell in Bi and $Bi_{1-x}Sb_x$. This is an equivalent notation for the $R\bar{3}m$ point group and simplifies XRD interpretation.

properties of the film. However, Bi films 4nm and below exhibit island mode growth making them non-continuous and therefore inviable for ex-situ electrical measurements.

The transition of $Bi_{1-x}Sb_x$ from an (001) oriented film to an (012) orientation between 4% and 9% Sb has not been previously observed, and carries with it significant changes in the expected material properties of the films. As $Bi_{1-x}Sb_x$ exhibits a rhombohedral crystal structure, the effective mass is anisotropic and so will change between the two orientations[55]. This change in the effective mass will affect the shape of the energy bands as well as the quantum confinement experienced by the films. The measured electrical effects of this crystal structure transition are further discussed in Chapter 3. Further measurements of the atomic spacing of these films, such as through STM, is necessary to ascertain their structure.

2.2.2 Composition of $Bi_{1-x}Sb_x$ Films

We have examined the composition of our epitaxial $Bi_{1-x}Sb_x$ films using both Electron dispersive X-ray spectroscopy (EDS) and X-Ray Photoemission Spectroscopy (XPS). The combination of these methods allows us to evaluate the incorporation of Sb into our films, as well as the ratio of Sb to Bi and the chemical state of the material. It is necessary to know the precise composition of our $Bi_{1-x}Sb_x$ films due to the composition-dependent band structure observed in $Bi_{1-x}Sb_x$.

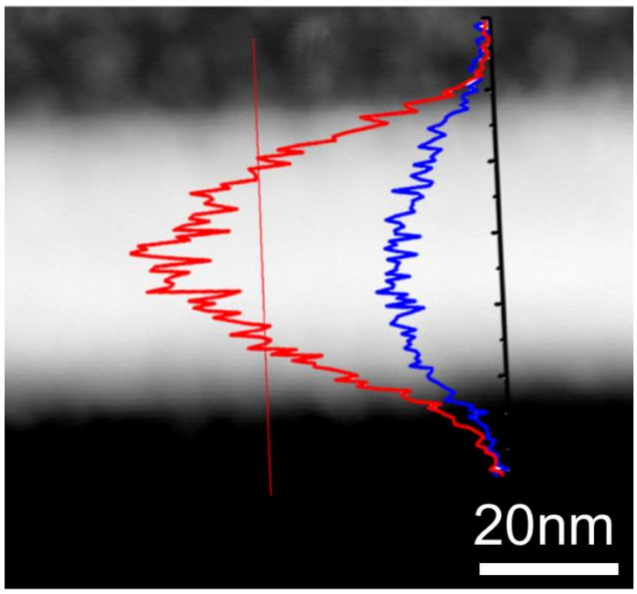

Figure 2.3: TEM and EDS measurements of a 40 nm $Bi_{0.75}Sb_{0.25}$ film

EDS measurements acquired through transmission electron microscopy (TEM) are used to examine the antimony concentration across an area of the sample (Figure 2.3). In this measurement, a high-energy beam of electrons is used to excite X-rays from a sample. These X-rays are measured by a detector and their energies are used to identify the element from which it was emitted. Figure 2.1 shows the even distribution of Sb throughout the epitaxially-grown film. This measurement indicates that the film does not exhibit phase or surface segregation of the Sb. This is important as it indicates that the incorporation of Sb is not creating additional defects, grain boundaries, or stacking faults in the films which reduces the likelihood that the film will exhibit uncharacteristic behavior.

Although EDS measurements are useful to examine the distribution of Sb and Bi atoms within the epitaxial films, they are not surface-sensitive enough to quantify the composition of the films. EDS typically excites X-rays from atoms in depths up to multiple microns, which makes excitations from the atoms in our 10-50 nm films a very small

percentage of the X-rays detected. Due to this, XPS is used instead to quantify the ratio of Bi to Sb. In addition, XPS has the benefit of being able to distinguish between oxidized and unoxidized material, making it a useful tool in examining the oxidation effects in our films.

XPS is a method of calculating the binding energy of atoms on a surface. XPS uses X-rays to excite photoelectrons which have kinetic energies related to the binding energy of the atom they were excited from. From this information, the elemental identity and chemical state can be determined. XPS is particularly useful for materials that oxidize, such as Bi, as the binding energy of a Bi-Bi bond and a Bi-O bond are distinguishable – allowing approximation of the ratio of metallic to oxidized material at the surface.

Our film composition is measured using a Kratos XPS system with an ultra-high vacuum measurement chamber and a detection depth of 2-8 nm. Analysis of the resulting spectra is performed using CasaXPS. The background is fit using a Shirley background and individual binding energy peaks are fit to a Gaussian-Lorentizan model. The adventitious carbon peak is used as a reference for all binding energy measurements. Peak fits are converted to atomic percentages using a machine-specific relative sensitivity factor. As one half of the Sb 3d spin-orbit doublet overlaps with an oxygen energy peak, this peak is eliminated from analysis. Therefore, all composition fits are performed on the non-overlapping doublet with an adjusted sensitivity factor to correct for the missing peaks. A representative spectra showing the four Bi peaks and two Sb peaks used to identify the atomic ratios in our samples is shown in Figure 2.4.

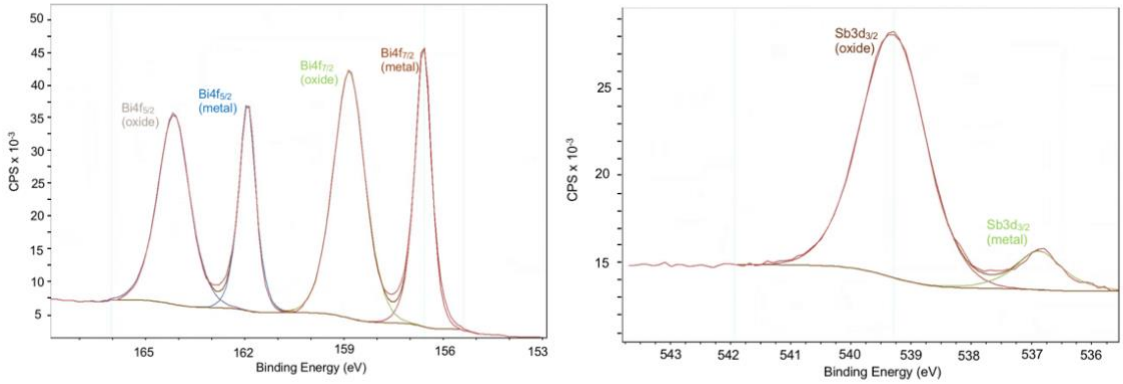

Figure 2.4: Representative XPS measurement showing the binding energy of a.) Bi-Bi and Bi-O and b.) Sb-Sb and Sb-O, both of which exhibit a spin orbit doublet

Using XPS analysis, we have found that the percentage of Sb in our films varies radially by approximately 20% across the wafer. This may be due to variations in the substrate temperature during growth. We have found that the variation of Sb is negligible within a circle of radius approximately 2 cm around the center point of the wafer, thus all electrical characterization described in later chapters is measured from this area.

We have examined the measured alloy composition of the $Bi_{1-x}Sb_x$ films as a function of the ratio of Sb beam equivalent pressure (BEP) to total Sb and Bi BEP during growth (Figure 2.5a). The BEP is proportional to the flux of the material at the sample surface and hence the growth rate. From this study, we can conclude that the percentage of Sb found in our films is approximately twice that of the percentage of Sb contributing to the BEP during growth. This is likely due to the incorporation of Sb as Sb-Sb bonded molecules rather than single atoms.

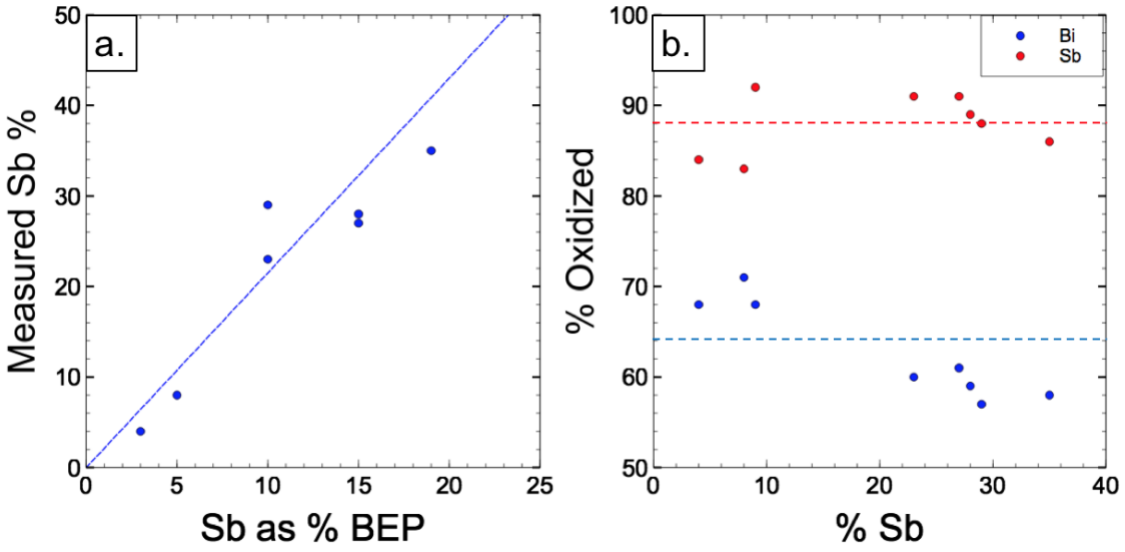

Figure 2.5: a.) Measured percentage of Sb in $Bi_{1-x}Sb_x$ vs. anticipated percentage of Sb based on growth BEP. b.) Percentage of O-bonded Bi and Sb vs. film composition in the surface 2-6 nm of the film (dotted lines are guide to the eye)

XPS measurements of $Bi_{1-x}Sb_x$ samples indicates the presence of larger ratio of Sb-O bonds to total Sb bonds compared to the ratio of Bi-O bonds to total Bi bonds (Figure 2.5b). This indicates that Sb may oxidize faster than Bi which is consistent with Sb oxide formation being relatively more energetically favorable than Bi oxide formation. The heat of formation of Sb_4O_6 is reported as -1440 kJ/mol while that of Bi_2O_3 is -574 kJ/mol. The reported alloy compositions are calculated using the total atomic percentage of Bi and Sb regardless of their bonding. This will more accurately reflect the composition *in situ* during growth, as well as the unoxidized film composition assuming a self-terminating oxide.

Although the measured percentage of oxidization is very large, this is primarily due to the surface sensitivity of the measurement method. We have been unable to identify an oxide layer using X-ray reflectivity (XRR) measurements of the films, which implies that the oxide layer is less than 2 nm thick. This indicates that the effect of oxidation in thicker

films should be minimal. In addition, electrical measurements performed *in situ* on both Bi and $Bi_{1-x}Sb_x$ are in good accordance with our values, indicating that the films transport behavior is robust to oxidation[42], [52].

Chapter 3: Transport in Quantum Confined Bi and $Bi_{1-x}Sb_x$

In this chapter we discuss the transport properties of quantum-confined Bi and $Bi_{1-x}Sb_x$ thin films. We identify the number and nature of channels contributing to transport using Hall resistance measurements. We also examine the thickness and temperature dependent transport in both Bi and $Bi_{1-x}Sb_x$ and discuss the origins of notable transitions as they correlate with a quantum confined band structure and metallic surface states. We demonstrate the unique semiconducting nature of previously unobserved (012) oriented $Bi_{1-x}Sb_x$. In addition, we find that electronic properties of Bi are surprisingly robust to oxidation as our measurements are in good agreement with those found in literature for *in situ* experiments[56]. Finally, we probe the influence of the large spin-orbit interaction in the magnetoresistance behavior of Bi through the observation of weak anti-localization and attempt to identify the nature of the channels contributing to this feature.

3.1 VAN DER PAUW METHOD

All transport measurements reported here are taken using the van der Pauw (vdP) method. The films are cleaved into approximately square samples of length 7mm-12mm. Contacts are created on each corner of the samples using indium-tin solder for all as-grown film and are deposited using a shadowmask for delaminated samples. The sheet resistance of the film is measured with 4-point probes on the corners of the sample as shown in figure 3.1. Contact size must be small relative to the total sample size for small measurement error.

Temperature-dependent sheet conductance measurements are performd with an Ecopia HMS-3000 Hall Measurement System that is cooled by liquid nitrogen to 77K and has a fixed magnet of 0.558T. Magnetoresistance measurements are taken using a Quantum

Design EverCool2 PPMS which can be cooled with liquid helium down to 2K and has a variable magnet that can supply a field up to 9T.

Both the Bi films and the $Bi_{1-x}Sb_x$ films are grown on highly resistive Si wafers. The Bi films are grown on lightly-doped p-type Si (111) wafers that are 350um thick and have a resistivity of 3500 ohm-cm. This results in a substrate sheet resistance of 1E5 ohms. The Bi films have a resistivity of approximately 1E-4 ohm-cm and so will have a sheet resistance that less than 0.1% of that of the substrate for films in the thickness regime we grow, allowing us to ignore the substrate contribution. The $Bi_{1-x}Sb_x$ films are grown on 350um thick intrinsic Si (111) with a resistivity of approximately 2E5 ohm-cm. As the resistivity of the $Bi_{1-x}Sb_x$ films is approximately 1E-3 ohm-cm, the transport contribution due to the substrate should be negligible.

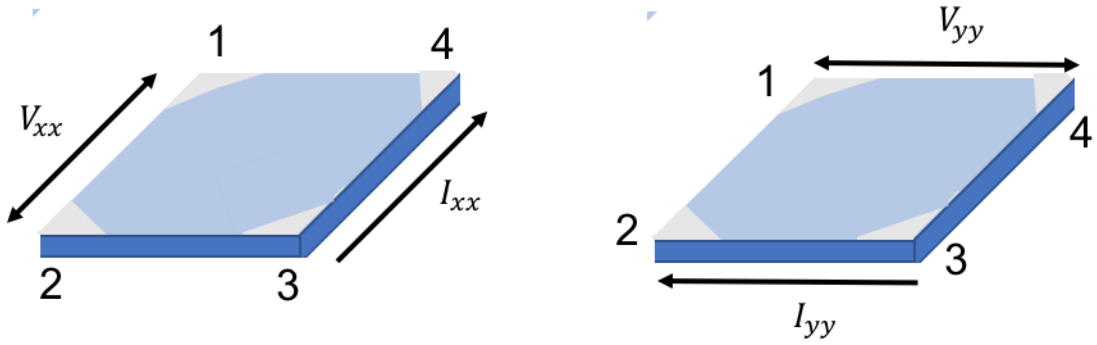

Figure 3.1: The van der Pauw method for sheet resistance measurement

The measurements can then be fit to the van der Pauw equation to obtain the sheet resistance R_{sh} of the film:

$$e^{-\frac{\pi R_A}{R_{sh}}} + e^{-\frac{\pi R_B}{R_{sh}}} = 1$$

$$R_A = \frac{R_{12,34}+R_{34,12}+R_{21,43}+R_{43,21}}{4},\ R_B = \frac{R_{23,14}+R_{14,23}+R_{32,41}+R_{41,32}}{4}$$

Where $R_{ij,kl} = \frac{V_{ij}}{I_{kl}}$, $V_{ij} = V_j - V_i$, and I_{kl} is the current going into contact k and coming out of contact l.

This method automatically corrects for deviations of the sample geometry from a perfect square and does not require precise knowledge of the length and width of the samples. In addition, the above methodology can be used unmodified for measurements of transferred films of arbitrary geometry[57]. We correct for any variations in the I-V behavior by taking the reciprocal measurements and averaging. We also correct for any voltage offsets, such as those from thermoelectric effects by reversing the polarity of the measurements and averaging. This especially important for Bi and $Bi_{1-x}Sb_x$ because of their large thermoelectric figure of merit.

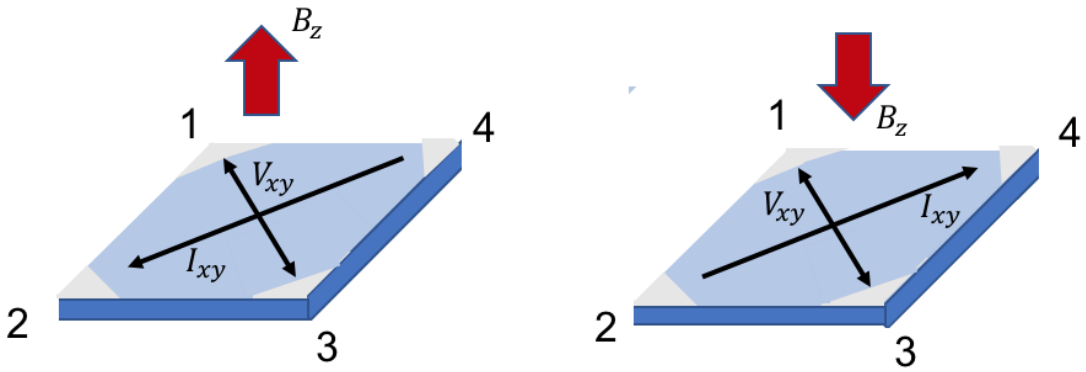

Figure 3.2: The van der Pauw method for magnetoresistance and hall resistance measurement

By switching the orientation of the magnetic field, we can measure both the longitudinal magnetoresistance:

$$R_{MR} = \frac{R_{xx}(+B) + R_{xx}(-B))}{2\,R_{xx}(0)}$$

and the hall resistance:

$$R_H = \frac{1}{2}(R_{xy}(+B) - R_{xy}(-B))$$

Where $R_{xy} = R_{24,13} + R_{42,31} + R_{31,42} + R_{13,24}$ and $R_{ij,kl}$ is defined as before.

For all measurements reported here, the magnetic field is oriented along the direction of film growth and the Hall voltage (R_H) is measured such that a positive R_H corresponds to p-type transport and a negative R_H corresponds to n-type transport. As multiple carriers contribute to the transport behavior in Bi, R_H is magnetic field dependent. Due to this, a simple hall measurement at fixed field is not sufficient to ascertain the mobility or carrier concentration in the Bi films.

3.2 HALL MEASUREMENTS AND TRANSPORT CHANNELS[2]

As the band gap in our epitaxially grown Bi films arises from quantum confinement instead of bulk material properties, both the conduction band and the valence band contribute to the transport behavior as they would in semimetallic Bi[58], [59]. In addition, the well-defined presence of surface states in Bi contributes another transport channel of unconfirmed carrier identity[60].

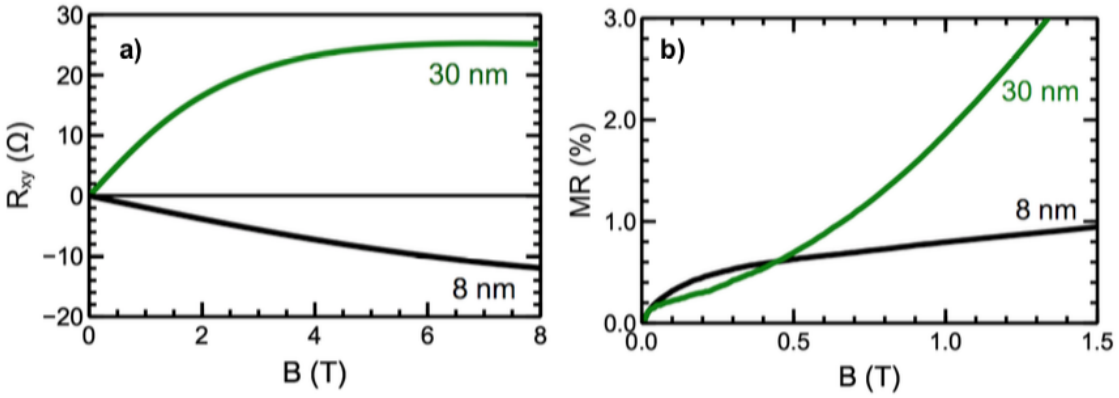

Figure 3.3: a.) Hall measurements and b.) magnetoresistance measurements of 8 and 30nm Bi films with varying field measured at 2K

[2] This section includes data and analysis completed by E. S. Walker as a part of her doctoral dissertation. Further discussion can be found in [53]

The negative hall resistance (Figure 3.3a) seen in the 8nm Bi film is indicative of n-type dominated transport while the positive Hall resistance seen in the 30nm Bi film is indicative of p-type transport. The transition between these two carrier regimes is reflective of the transition in the transport behavior seen around a film thickness of 15 nm. The magnetoresistance (Figure 3.3b) of both the 8 nm and 30 nm films exhibit a low-field dip characteristic of weak antilocalization (WAL) which occurs due to strong spin-orbit coupling in the films. The shift around 0.25 T from WAL-like behavior to quadratic behavior typical of traditional magnetoresistance has been previously observed in Bi[61]. A better understanding of the origins of the different contributions to the Bi MR might be achieved through parallel magnetic field measurements as described by Wang et al.[62]. Above 1 T, the magnetoresistance is defined by magnetic field disruption of the cyclotron trajectory of individual electrons. The cyclotron magnetoresistance can be mathematically represented as [57]:

$$\%MR \propto 1 + (\mu_{MR}B)^2$$

The WAL cusp is not reflective of typical magnetoresistive behavior and is thus eliminated in our fitting. Fitting the WAL feature is discussed further in section 3.8.

Hall measurements (R_{xx} and R_{xy}) of 8nm and 30nm Bi films have been fit to both 2-band and 3-band carrier models using the conductivity formulas:

$$\sigma_{xx} = \sum_i \frac{n_i e \mu_i}{1 + \mu_i^2 B^2}$$
$$\sigma_{xy} = \sum_i \frac{S_i n_i e \mu_i^2 B}{1 + \mu_i^2 B^2}$$

Where i is the index for each carrier, μ_i is he mobility of each carrier type, B is the magnetic field applied, and S_i is a sign term which corresponds whether the carriers are electrons or holes.

We apply these models to our hall and longitudinal resistance measurements by converting our measured resistance values to sheet conductance using the conductivity tensor and then converting to conductivity.

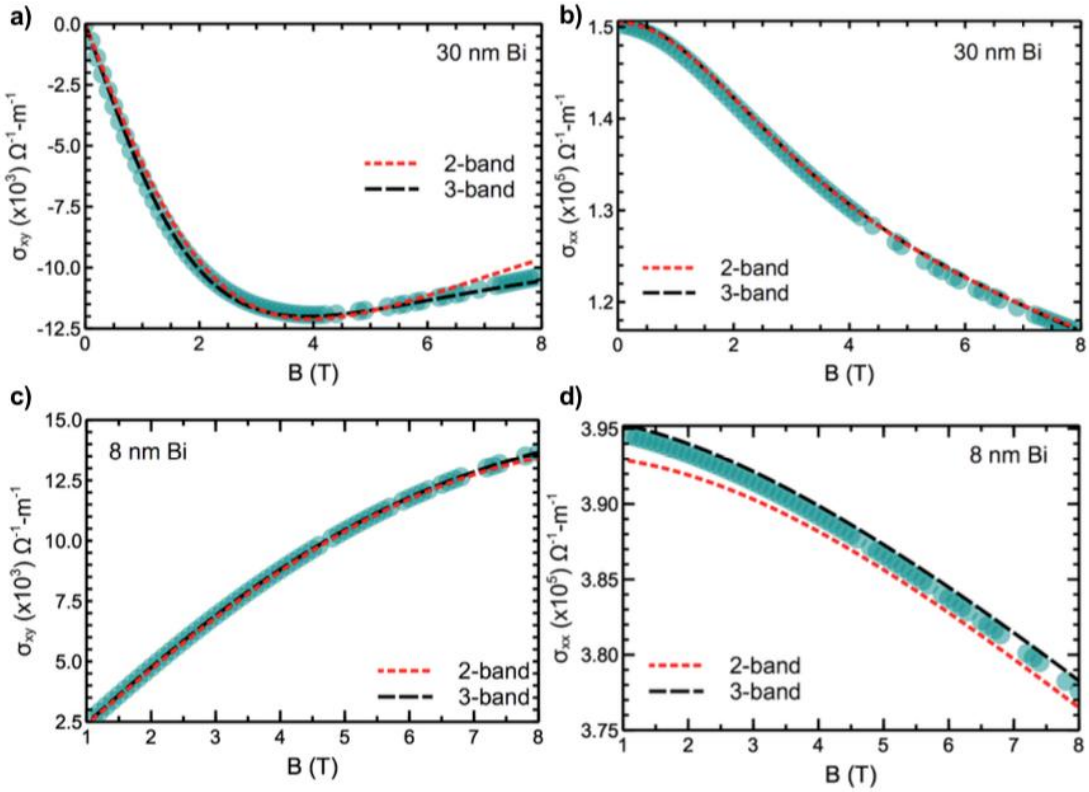

Figure 3.4: Hall measurement fits to 2-band and 3-band models for a.) 30nm Bi film σ_{xy}, b.) 30nm Bi film σ_{xx}, c.) 8nm Bi film σ_{xy} and d.) 8nm Bi film σ_{xx}

We simultaneously fit both the σ_{xx} and the σ_{xy} values to reduce error. Low fields are excluded from the fit due to the WAL feature. The carrier concentrations and mobilities are summarized in the Table 3.1 and 3.2.

d(nm)	$\boldsymbol{p_1}$ $(\boldsymbol{cm^{-3}})$	$\boldsymbol{n_1}$ $(\boldsymbol{cm^{-3}})$	$\boldsymbol{p_2}$ $(\boldsymbol{cm^{-3}})$
8	1.1 x 10^{19}	3.8 x 10^{19}	N/A
30	1.3 x 10^{19}	1.5 x 10^{19}	5.7 x 10^{17}

Table 3.1: Carrier Concentrations for 8nm and 30nm Bi films

d(nm)	$\boldsymbol{\mu_{p1}}$ $(\boldsymbol{cm^2/Vs})$	$\boldsymbol{\mu_{e1}}$ $(\boldsymbol{cm^2/Vs})$	$\boldsymbol{\mu_{p2}}$ $(\boldsymbol{cm^2/Vs})$
8	365	300	N/A
30	303	674	2930

Table 3.2: Carrier mobilities for 8nm and 30nm Bi films

Our fitted values for carrier concentrations and mobilities are very large as is expected for Bi. Bulk electron and hole carrier concentration in semimetallic Bi films at low temperature has been found to be 2 x 10^{17} using a two-band model[55]. This value is approximately two orders of magnitude smaller than our measurements. This may be due to the modification of the Bi energy band structure due to quantum confinement. In addition, we identify the surface states, responsible for the 3rd band of transport, as holes as seen in Table 3.1. Our measurements indicate positive Hall resistance for the 30nm film and a negative Hall resistance for the 8nm film. As we expect the surface states to dominate the transport behavior of the 8nm films, it is unexpected that the Hall resistance would indicate n-type behavior. However, we find that the 8nm films can be accurately fit using a 2-band conductivity model with one electron channel and one hole channel. This may be due to hybridization of the bulk and surface states in very thin films, which would result in fewer distinguishable bands[63]. Clarification of this phenomena might be achieved through future gated measurements.

3.3 HIGHLY TUNABLE ELECTRICAL PROPERTIES

The combination of a thickness-dependent bandgap resulting from quantum confinement and metallic surface states makes Bi's transport behavior very unique to study[32]. $Bi_{1-x}Sb_x$ is predicted to exhibit a similar thickness-dependent band gap as well as a composition dependent band structure which is topologically insulating in compositions from 7% to 22% Sb[5]. The uniquely long de Broglie wavelength seen in Bi allows these quantum confinement effects to be observed in films as thick as 200 nm, allowing these effects to be studied at long length scales[34]. These quantum confinement effects cause the band gap to be inversely dependent on the square of the thickness of the material, as if the electron wavefunction is confined in an infinite quantum well. $Bi_{1-x}Sb_x$ is theorized to demonstrate similar quantum confinement effects[49]. In addition, alloying Sb with Bi allows for the introduction with another degree of freedom in the film properties. The thorough characterization of these effects will facilitate the design of these films for specific applications.

The temperature-dependent transport behavior observed in Bi and $Bi_{1-x}Sb_x$ films can be analyzed using basic knowledge of temperature-dependent transport in semiconductors/insulators and metals. The conductivity of a metal will decrease with temperature as the higher energy of the electrons will cause the mean free path to decrease and scattering events to occur more frequently. Conversely, the conductivity of an insulator or semiconductor will increase with temperature as more electrons are able to scale the bandgap as energy is increased. In the case of both Bi and $Bi_{1-x}Sb_x$, both the bulk insulating and metallic surface will affect the transport behavior of the material. As the films get thinner, we experience two competing effects. The metallic surface states will account for a larger percentage of the carriers in the film thus making the transport behavior appear more metallic. Meanwhile, the quantized energy levels will be pushed farther apart as the

confinement direction gets smaller – resulting in a larger bandgap and more insulating transport behavior.

3.3.1 Quantum Confinement and Surface States in Bi

As Bi experiences quantum size effects at notably large film thicknesses, we can easily tune the band gap of the film to create custom devices. This may be especially useful in accessing the Rashba spin-split surface states for development of spintronic devices[32].

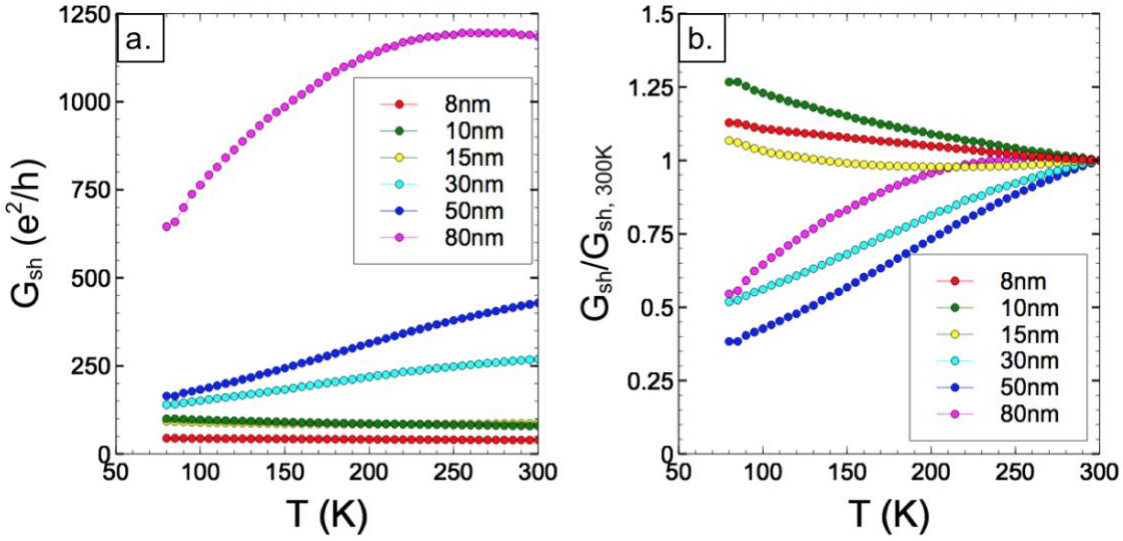

Figure 3.5: Bi temperature dependent sheet conductance measurements a.) in conductance quanta b.) normalized to value at 300K

The increase in conductance with temperature in films 30nm and thicker is indicative of the semiconducting behavior of the bulk states. The transition from semiconducting behavior to metallic in films less than 30nm is attributed to Bi's prominent surface-state transport[56].

As the film thickness decreases, we expect the two opposing contributions to conductance behavior to change as well. The semiconducting behavior of the bulk states is due to the quantum confinement of the carriers and thus the intrinsic bandgap of the Bi

films will increase with decreasing film thickness as $\Delta Eg \propto \frac{1}{d^2}$. The bulk-associated conductivity will thus decrease with decreasing film thickness as $\sigma_{bulk} \propto e^{-\frac{Eg}{2kT}}$. Counteracting this, the metallic surface states do not exhibit a thickness-dependent term in their conductance, so as the film thickness increases, the measured sheet conductance will be proportionally more and more defined by the bulk carriers as $G_{sh} = \sigma_{bulk} d + G_{ss}$.

We can observe that the 80nm film appears less semiconducting compared to the 50nm, likely due to the reduced quantum confinement and thus decreased bandgap in thicker films. The opposite behavior, where the 30nm film appears less semiconducting than the 50nm film, can be attributed to the surface states being a large enough contribution to the overall conductance that the increase in metallic behavior dominates over the increase in semiconducting behavior. This indicates that the contribution due to the surface states only becomes small enough to be neglected between 50nm and 80nm.

Similarly, in films thinner than 30nm, the transport behavior is dominated by the metallic surface states. We can see a monotonic increase in the slope of $G_{sh} / G_{sh,300K}$ vs. T measurements with decreasing thickness in films from 15nm to 10nm, which can be attributed to the increasing influence of the metallic surface states over the semiconducting bulk states as the film gets thinner. However, the 8nm film exhibits behavior that is less metallic than the 10nm film – indicating that the bandgap of the bulk states has increased more than the contribution due to surface states with the change in film thickness. This matches with previously predicted behavior where the surface and bulk bands hybridize between 8-10nm and with the similar reduction of carrier channels seen in our Hall resistance measurements[63]. This allows us to tentatively split the transport behavior of quantum confined Bi (001) into 6 regimes as shown in Table 3.3.

Bi film thickness (nm)	Transport behavior
>180	Bulk semimetallic
80-180	Semiconducting (quantum confined), n-type
15-80	Mixed semiconducting and metallic, semiconducting (quantum confinement) dominant, n-type
8-15	Mixed semiconducting and metallic, metallic (surface states) dominant, n-type
2-8	Hybridized semiconducting and metallic, n-type
<2	Unknown

Table 3.3: Bi film thickness transport regimes

3.3.2 Alloy Composition and Quantum confinement in $Bi_{1-x}Sb_x$ Films

$Bi_{1-x}Sb_x$ films exhibit quantum size effects at similar length scales to Bi and thus the bandgap of these films can be similarly tuned through varying the film thickness. In addition, the band structure of $Bi_{1-x}Sb_x$ is known to be composition dependent, which allows another degree of . The epitaxially grown $Bi_{1-x}Sb_x$ films discussed in this document fit into come in two distinct forms – the (001) and the (012) orientation, each with unique electrical properties. The transition between these two orientations is seen to occur between 4% and 9% Sb.

We can observe that the temperature-dependent sheet conductance of (001) oriented $Bi_{0.96}Sb_{0.04}$ is nearly identical to that seen in pure epitaxial Bi in 10 nm films (Figure 3.6a). As the films get thicker, however, the transport behavior begins to diverge with $Bi_{0.96}Sb_{0.04}$ appearing more semiconducting than pure Bi. This may indicate that the contribution of surface states is very similar in both Bi and (001) $Bi_{0.96}Sb_{0.04}$, although their bulk band structure differs. The conductivity minima seen at low temperatures in Figure

3.6b are a consequence of the competition between the bulk and surface state transport. These minima may be useful in ascertaining the relative contributions of the surface and bulk states to the overall transport behavior.

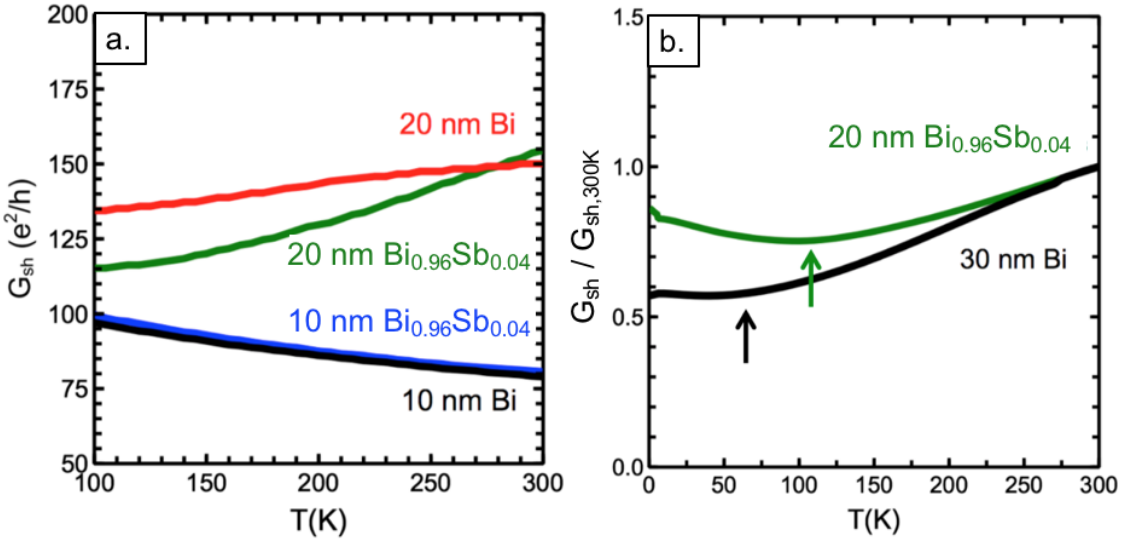

Figure 3.6: Comparison of temperature-dependent sheet conductance of Bi and $Bi_{0.96}Sb_{0.04}$ films a.) in units of conductance quanta and b.) normalized to the value at 300K

Temperature-dependent sheet conductance measurements of different composition $Bi_{1-x}Sb_x$ films indicate that there are two clear regimes of transport behavior – that seen in films of less than 4% Sb composition, and that seen in films of greater than 9% Sb composition (Figure 3.7). These regimes correlate with those of (001) orientated $Bi_{1-x}Sb_x$ and (012) orientated $Bi_{1-x}Sb_x$ respectively (see Chapter 2). The (012) oriented films appear semiconducting with temperature, while (001) oriented films appear metallic with temperature. Varying the composition within these regimes does not appear to significantly change the bandgap or surface state contribution as evidenced by the very similar temperature-dependent transport behavior seen between 9% Sb and 30% Sb.

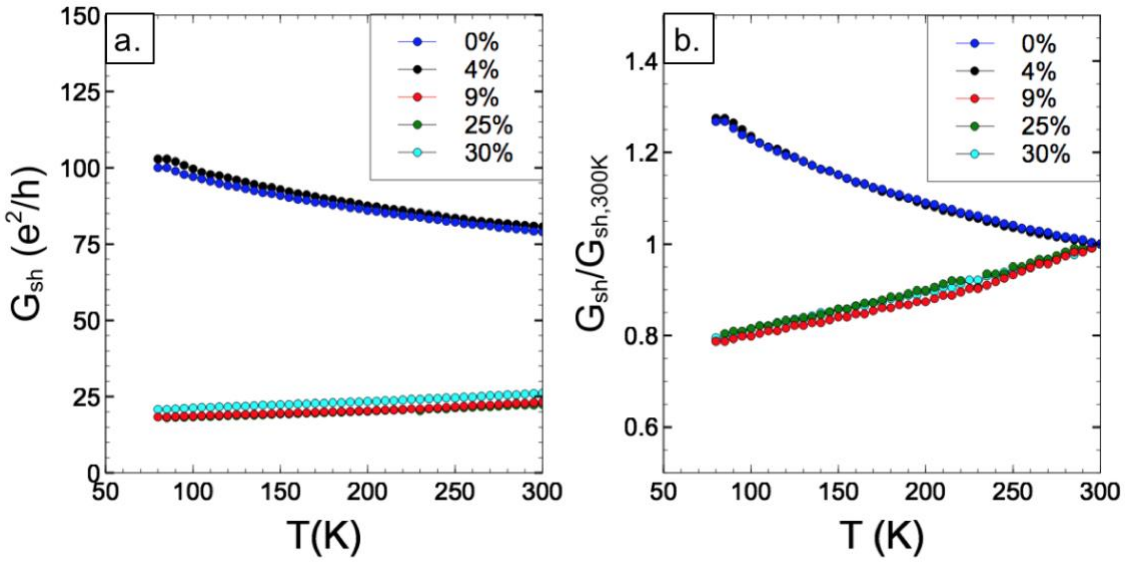

Figure 3.7: 10nm $Bi_{1-x}Sb_x$ temperature-dependent sheet conductance measurements at different compositions a.) in units of conductance quanta and b.) normalized to the value at 300K

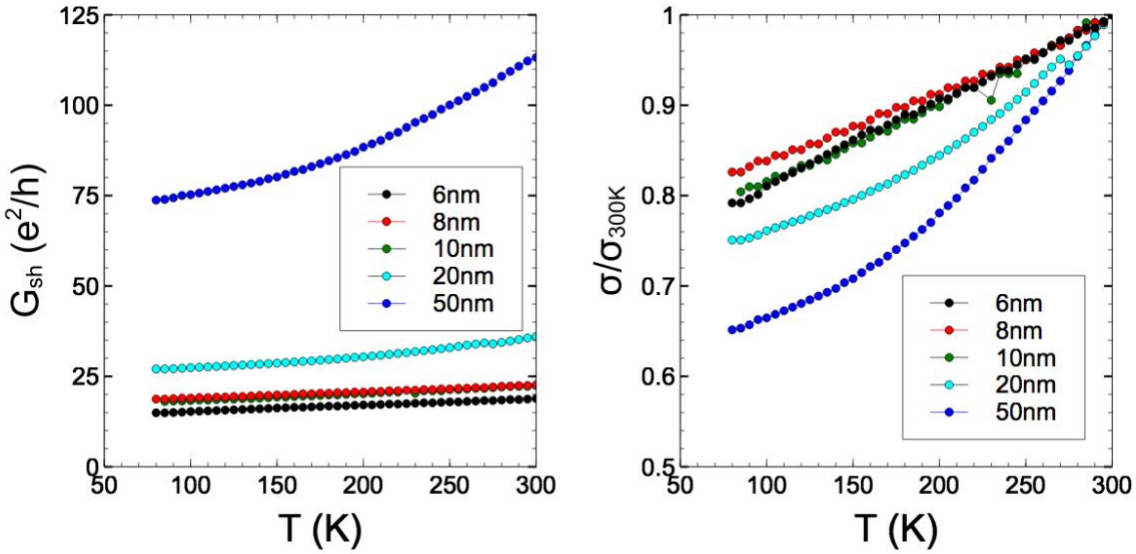

Figure 3.8: $Bi_{0.75}Sb_{0.25}$ temperature-dependent sheet conductance at different film thicknesses a.) in units of conductance quanta and b.) normalized to the value at 300K

In contrast to the Bi films, we can see that the (012) oriented $Bi_{0.75}Sb_{0.25}$ films are semiconducting down to 6 nm (Figure 3.8). This indicates that, while it's not necessarily true that there are no surface states in the (012) oriented $Bi_{1-x}Sb_x$ films, they are likely no longer dominantly metallic. We can also observe that the slope of the sheet conductance vs temperature decreases as the film thickness is decreased. This correlates with an decrease in bandgap as the film thickness is decreased – which is the opposite of the expected behavior in quantum confined films. This implies that there is some component in the transport that has a greater influence in the thinner films – indicating that surface states remain. These surface states appear to exhibit behavior which causes the overall sheet conductance to decrease with temperature. However, these surface states do not appear to dominate the transport behavior even in films as thin as 6 nm as there is no transition to metallic behavior seen as is present in pure Bi films. This may stem from hopping-style transport occurring in the surface antimony oxide and would account for this behavior not being present in the pure Bi films.

Despite the crystalline orientation change, these conductivity measurements agree well with those reported for $Bi_{1-x}Sb_x$(001) films on GaAs(111), which reported values between 1 – 4 $x10^3\Omega^{-1}cm^{-1}$ for 0-80% Sb films under 25 nm at 270 K[52].

3.3.3 Analysis of Transport

Due to the negligible influence of the surface states on the conductance of the 80nm Bi film, we can fit the film to the simple thermal activation function expected for a semiconductor:

$$\sigma = \sigma_0 e^{-\frac{E_g}{k_B T}}$$

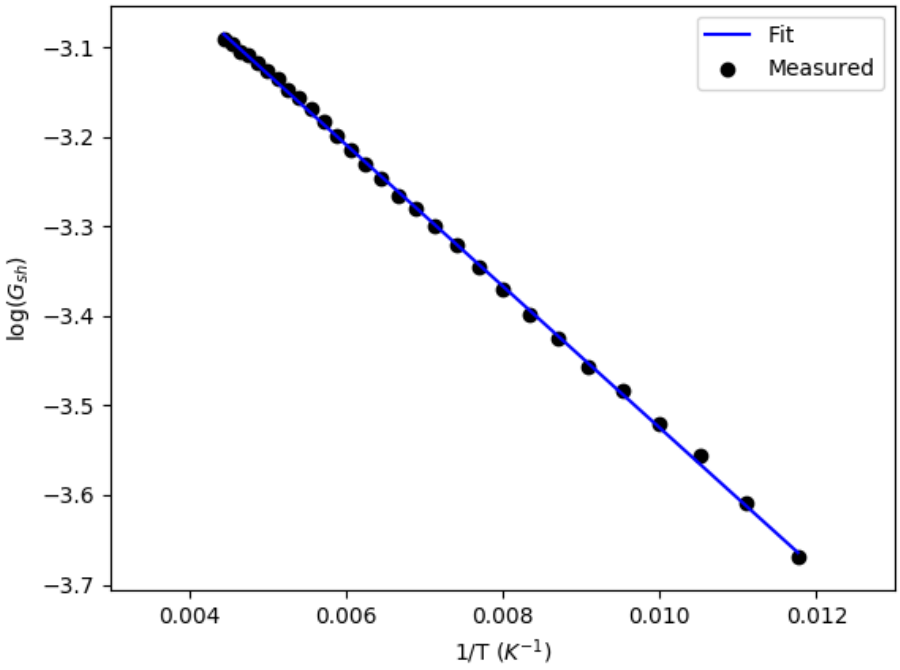

Figure 3.9: Thermal activation fit of 80nm Bi film

This results in a calculated bandgap of 13.6 meV (Figure 3.9). Attempts at fitting the bandgap of the thinner films proves nontrivial as the surface state contribution is significant so the conductance cannot be cleanly modeled by a simple thermal activation function. This requires that further analysis must be performed to ascertain the thermal dependence of the surface states for an accurate model of the temperature-dependent transport of Bi films to be reached.

We can attempt to isolate the surface state (SS) contribution to the conductance from the overall conductance of the films by using the equation:

$$G = G_{SS} + \sigma_{bulk} d$$

Where G_{SS} is the conductivity contribution due to surface states which should be thickness independent, and σ_{bulk} is the conductivity contribution due to the bulk carriers.

We perform a linear regression on hall measurements taken from Bi and $Bi_{1-x}Sb_x$ films of thicknesses ranging from 6nm to 50nm. The y-intercept of this linear regression will then correspond to the film thickness=0 point at which only surface states can contribute to the transport of the material.

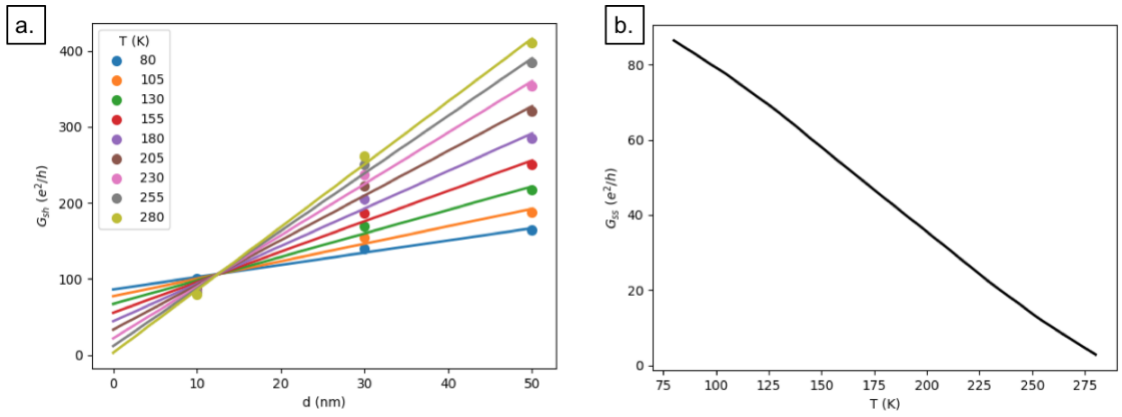

Figure 3.10: Conductance contribution of surface states for pure epitaxial Bi films a.) fit of conductance vs. film thickness b.) calculated surface state contribution vs. temperature

Our fits match the thickness dependent behavior of the film conductance to a standard error of less than 2% for both Bi and $Bi_{1-x}Sb_x$ films. The decrease of the surface state contribution to below zero is due to the comparatively crude approximation we have made to disregard the effects of quantum confinement (Figure 3.10a). We can observe that the conductance of the surface states decreases with increasing temperature which matches the anticipated metallic nature of surface states in Bi (Figure 3.10b).

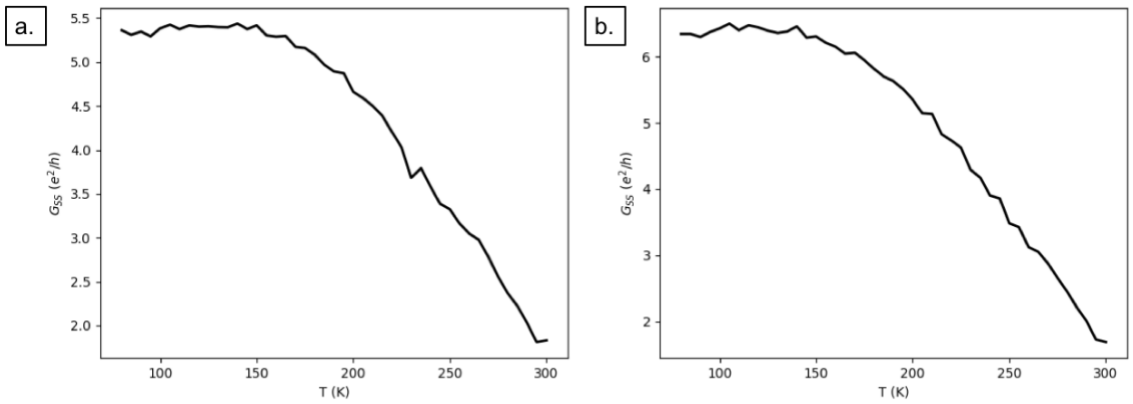

Figure 3.11: Conductance contribution of surface states for a.) $Bi_{0.75}Sb_{0.25}$ and b.) $Bi_{0.70}Sb_{0.30}$ films.

The temperature-dependent sheet conductance of surface states in $Bi_{1-x}Sb_x$ (Figure 3.11) is calculated in the same manner as for pure Bi. Although the overall behavior of the surface states is decreasing with temperature, which indicates they are metallic, the lack of transition to metallic-dominated transport in the $Bi_{1-x}Sb_x$ films indicates that this is not the case. In addition, the leveling out of the conductance at temperatures below 140K indicates that the transport behavior of the surface states in the $Bi_{1-x}Sb_x$ films is no longer purely metallic. This may be due to some kind of oxidation effects on the surface. In addition, as these films are (012) oriented, which has been not been previously studied by other groups to our knowledge, this transport behavior may have not been previously observed.

The prior calculations disregard the thickness-dependent bandgap present in both Bi and $Bi_{1-x}Sb_x$ in the thickness regime studied. A more rigorous treatment of the transport behavior can be derived using the infinite well approximation of the film bandgap in the z-direction:

$$\Delta E_g = 2\frac{\pi^2\hbar^2}{2\,m^*\,d^2}$$

A more accurate picture can be gathered using a modified formula from[64]:

$$G_{sh} = d\ \sigma_0 e^{-\frac{\left(\frac{E_g}{2}+\frac{b}{d^2}\right)}{k_B T}} + \frac{1}{\rho_0 + sT}$$

Where E_g is the bulk band overlap of semimetallic Bi (approximately -38 meV), d is the film thickness, ρ_0 is the surface residual resistivity and sT is the electron-phonon induced resistivity which exhibits a linear dependence on temperature [65].

3.4 MAGNETOCONDUCTANCE MEASUREMENTS AND WEAK ANTI-LOCALIZATION

It is well known that weak localization (WL), a quantum mechanical interference phenomena visible in weakly disordered systems at low temperatures, causes a sharp increase in the magnetoresistance (MR) of most non-magnetic materials at low fields[66]. The inverse, weak anti-localization (WAL), is a feature of MR seen in materials with strong spin orbit coupling where the negative interference of electron paths results in a sharp decrease in the MR at low fields[67]. The WAL feature is commonly studied in known topologically insulating materials as it can be indicative of non-trivial topological surface(s). This effect stems from the characteristic spin-momentum locking and π-Berry phase due to the odd number of Dirac points[24]. The π-Berry phase causes interaction of time reversed electron paths to interact destructively instead of constructively which results in WAL phenomena[68].

The Rashba spin-orbit interaction, as is present in pure Bi, causes similar effect in the electron paths resulting in destructive interference and a WAL feature [69], [70]. As both of these effects belong to the symplectic universality class of disordered, systems which defines the modelling of this phenomena, it is very difficult to distinguish between topologically non-trivial states and topologically trivial surface states with Rashba splitting[71], [72]. The presence of a WAL feature in Bi's MR behavior is expected due to its Rashba spin-split surface states, and has been well established by experiment[61],

[63][73]. Although this feature cannot help distinguish the topological order of the material, its study can provide a greater understanding of number, behavior, and interactions of conductive surface channels contributing to transport.

MR measurements can be analyzed for both WAL and WL contributions to the transport behavior using the Hikami-Larkin-Nagaoka (HLN) equation[72]:

$$\Delta\sigma = \frac{\alpha e^2}{2\pi^2\hbar}\left[\Psi\left(\frac{1}{2}+\frac{\hbar}{4el_\phi^2 B}\right) - \ln\left(\frac{\hbar}{4el_\phi^2 B}\right)\right]$$

Where Ψ is the digamma function and l_ϕ is the spin coherence length.

The alpha parameter in the HLN equation indicates the number and type of states affecting the quantum interference behavior in the transport. An alpha parameter of 0.5 is characteristic of the symplectic class and is indicative of WAL, while an alpha parameter equal to -1 belongs to the unitary class and is indicative of WL behavior. Deviations from these values indicates multiple conduction channels typically arising from coupling of the surface states with bulk-states [74], [75].

This low-field fit (Figure 3.15) finds an α parameter of 0.17, and an l_ϕ of 214nm. The deviation of the α parameter value from the expected 0.5 for a single symplectic channel is indicative of a bulk contribution from either conventional MR or WL. The low value of the α parameter indicates that there is only one surface contributing to the transport even at this relatively small film thickness [76].

Further work is necessary to identify and fit the higher field features resulting from the conventional cyclotron MR term, influence of scattering as seen in the extended HLN equation, and interaction between the bulk and surface states [27]:

$$\Delta\sigma = \frac{\alpha e^2}{2\pi^2\hbar}\left(\left[\Psi\left(\frac{1}{2}+\frac{\hbar}{4el_\phi^2 B}\right) - \ln\left(\frac{\hbar}{4el_\phi^2 B}\right)\right] + 2\left[\Psi\left(\frac{1}{2}+\frac{\hbar}{4el_\epsilon^2 B}\right) - \ln\left(\frac{\hbar}{4el_\epsilon^2 B}\right)\right]\right)$$

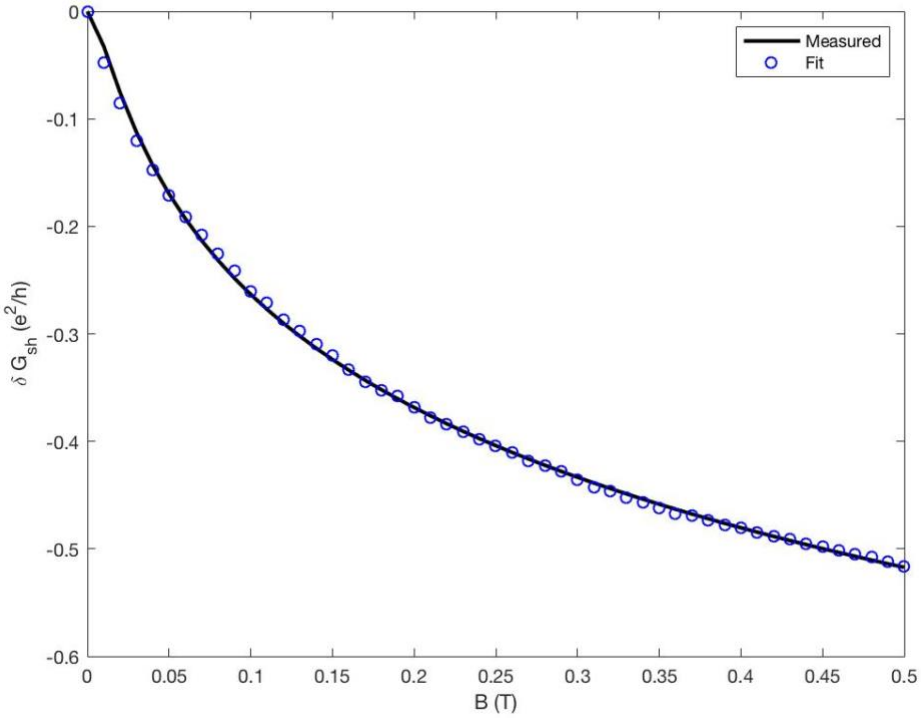

Figure 3.12: Low-field WAL feature fit for 8nm Bi film

Conclusive identification of the higher field features will require further measurements of films in the different projected thickness regimes outlined in section 3.3.1. These measurements will allow for greater understanding of the behavior when different channels are dominating the transport behavior. In addition, in-plane measurements may be useful to isolate the bulk contribution to the MR and gated measurements may be useful to explore the effects of coupling as the Fermi level is shifted[62], [77].

Chapter 4: Dry Transfer of Epitaxial Bi and $Bi_{1-x}Sb_x$ Thin Films[3]

In this chapter, we report the ability to transfer high quality films of Bi and $Bi_{1-x}Sb_x$ which retain their unique material and electrical properties using a thermal release tape dry transfer method. We demonstrate that this process is substrate-independent and facilitates the transfer small continuous ~10 μm x 10 μm areas of the films with nearly identical properties to as-grown films. This process has potential for use as a tool to allow further characterization of these materials' unique properties as well as for development of devices based on these properties. We discuss the potential origins of the weak adhesion of Bi to its epitaxial Si substrate, as well as the implications of weak adhesion for $Bi_{1-x}Sb_x$'s properties, such as the early stage growth of a puckered layer allotrope similar to that seen in Bi. Finally, we demonstrate the potential of Bi for use as a release layer to allow the transfer of other epitaxial films.

4.1 Motivation for Dry Transfer

Integration of Bi and $Bi_{1-x}Sb_x$ into spintronic devices is not possible without the ability to achieve high quality films on ferromagnetic substrates. Unfortunately, high quality single-crystalline growth of both of these materials is very substrate-limited due to lattice matching constraints[52], [54]. Due to this limitation, high quality epitaxial growth of these films on ferromagnetic substrates is likely to prove extremely difficult. Therefore, a method to transfer high quality films to arbitrary substrates is necessary.

In addition to the development of spintronic devices, the ability to transfer high quality epitaxial Bi and $Bi_{1-x}Sb_x$ films to other substrates would allow further

[3] Section 4.2 of this chapter includes work that was previously published by our group in E. S. Walker *et al.*, "Large-Area Dry Transfer of Single-Crystalline Epitaxial Bismuth Thin Films," *Nano Lett.*, vol. 16, 2016. The author did not contribute to this published work, but has expanded the study through the work presented in the rest of the chapter.

characterization of these films such as with strain measurements on flexible substrates, phonon dynamics measurements on transparent substrates, and backgated electrical measurements on insulating substrates. A simple mechanical method for delaminating these films may also be useful for creating an unoxidized surface for sensitive measurements that must be performed *in situ* such as angle-resolved photoelectron spectroscopy (ARPES) and scanning-tunneling microscopy (STM).

4.2 DOUBLE CANTILEVER BEAM TRANSFER AND ADHESION MEASUREMENT

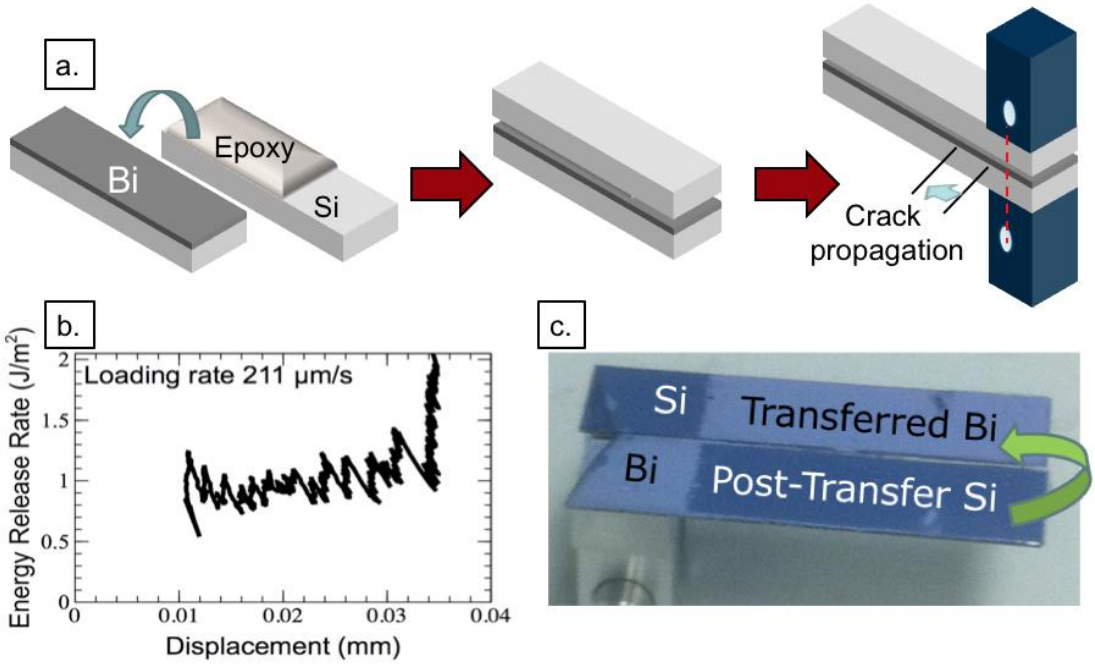

Figure 4.1: DCB transfer a.) process, b.) energy release rate, and c.) resulting Bi transfer

Previous work by our group has demonstrated the use of a double cantilever beam fracture method to delaminate epitaxial Bi from its growth substrate[78]. This method is commonly used for exfoliation of CVD-grown graphene[79], [80]. The DCB process uses

a 3-10 μm layer of low-viscosity EP-30 epoxy made by Masterbond to attach an 8mm x 40mm beam of epitaxially-grown Bi film to a handle Si substrate of the same geometry (Figure 4.1a). The epoxy is cured and then aluminum tabs are attached to the transfer stack. These tabs are used to slowly pull the two wafers apart at a set loading rate. This allows both the delamination of the Bi film onto the epoxy and the measurement of the load displacement as the Bi (001) is delaminated from the Si (111). This study found that the adhesion energy of Bi (001) on Si (111), taken as the average of the energy release rate, is surprisingly low at about 1 J/m^2.

This method has been shown to successfully transfer Bi films onto an epoxy on Si stack. In addition, we have found that it is possible to remove the epoxy from the Si with the Bi attached. Work is ongoing to transfer these samples to non-Si substrates by isolating the Bi films on epoxy and then dissolving epoxy using solvents.

4.2.1 Restrictions of DCB Transfer

The DCB transfer method has a few drawbacks which makes the development of a more general transfer process necessary. Mechanically, the DCB transfer is dependent on the Young's modulus of the epitaxial substrate and the handle substrate. If there is too much variation between the two values, there is an increased likelihood of shear effects resulting in crack propagation within the Bi film instead of along the Bi (001) / Si (111) interface. This reduces the potential handle substrates to those with very similar mechanical properties to Si (111), with transfers to Si (111) resulting in the highest quality film. In addition, the sample geometry is limited to those which can fit in the DCB setup – requiring a minimum sample size as well as precise cleaving of the epitaxial sample into this geometry. Growth of these films on substrates which have been pre-diced into the correct geometry are likely to be uneven due to the asymmetric shape of the beam. Beyond the

mechanical restrictions, these transfers result in an intermediary epoxy layer separating the Bi from the transfer substrate which must be removed before further processing or substrate-dependent measurements could be performed.

4.3 THERMAL TAPE TRANSFER

As an alternative transfer method, we have developed a process using thermal release tape in a similar way to which it is used for graphene exfoliation [81]. This transfer method removes the substrate material and geometry restrictions of the DCB fracture method and allows the direct transfer of the Bi film to new substrates without any intermediary layers or material which must be removed.

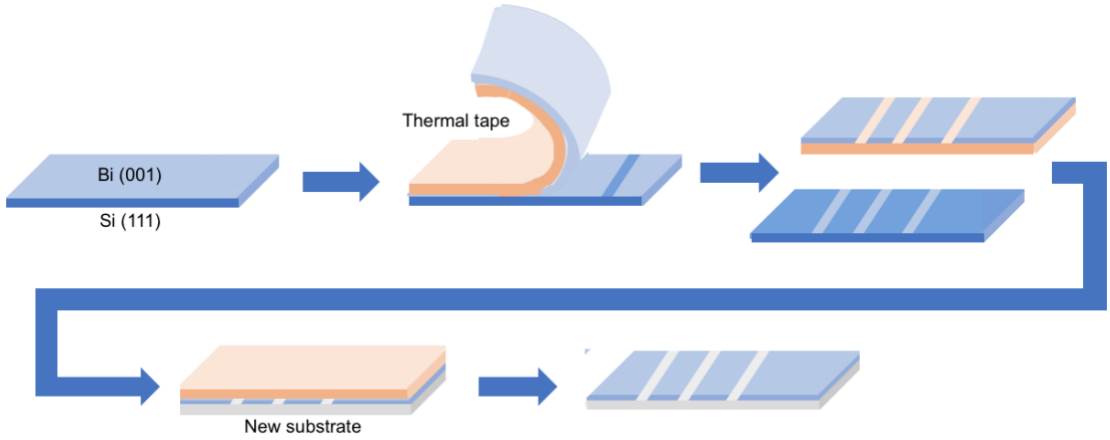

Figure 4.2: Thermal tape transfer method

The thermal release tape-based transfer method we have developed begins with an epitaxially grown Bi or $Bi_{1-x}Sb_x$ film on Si (111) as well as a new substrate intended to receive the transferred film. Both materials should undergo a solvent clean prior to the transfer process to remove any surface contaminants. The thermal tape is applied to the epitaxial film and then quickly peeled back at an approximate 135° angle from the plane of the substrate. This results in the delamination of the Bi or $Bi_{1-x}Sb_x$ film onto the tape.

The tape is then placed on the new substrate and pressed down firmly. The sample is heated to 210 °C resulting in the release mechanism of the tape being activated so that the film is deposited on the new substrate and the tape can be easily removed.

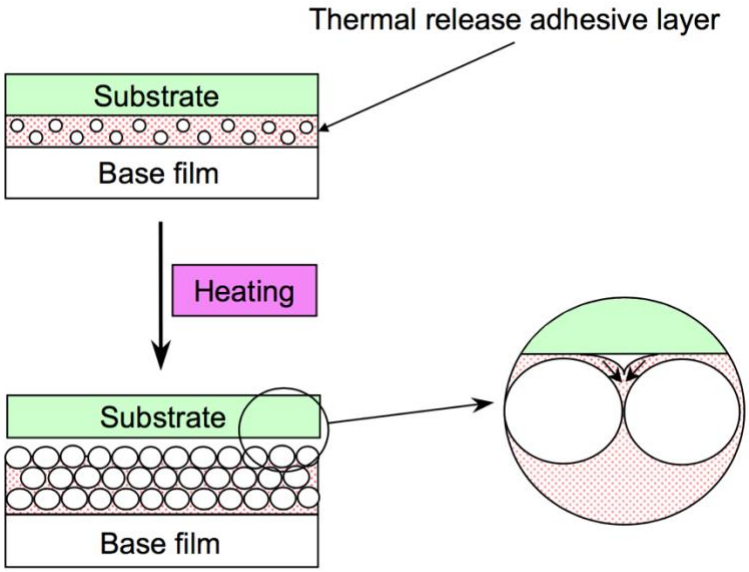

Figure 4.3: Thermal release tape mechanism from manufacturer Nitto Denko [82]

The use of tape for mechanical exfoliation is well established for use on graphene and other 2D and layered materials. Thermal release tape was invented for use as a temporary fixative to hold electronic components in place during processing, however it has seen rising popularity as tool for material exfoliation. The "release" mechanism in thermal release tape occurs due to foam spheres embedded within its pressure sensitive adhesive layer (figure 4.3). These spheres expand with the application of heat, causing a reduction in the contact area of the tape on the adherend which reduces the adhesive force holding the adherend to the tape. This allows for the easy removal of this tape with minimal adhesive residue left on the transferred film. All transfers are performed using thermal release tape No. 3195 manufactured by Nitto Denko unless otherwise noted. This tape has

an adhesion of 0.185N/mm on a PET film. The foam spheres embedded in this tape will expand at a minimum temperature of 90 °C, allowing for intermediary room temperature processing if desired.

Removal of the residue left by the thermal tape can be achieved by a simple solvent clean using acetone and isopropyl alcohol. O_2 plasma cleaning, as is used to remove tape residue from exfoliated graphene samples, is inviable for both Bi and $Bi_{1-x}Sb_x$ due to their propensity to oxidize.

4.3.1 Transfer of Epitaxial Bi

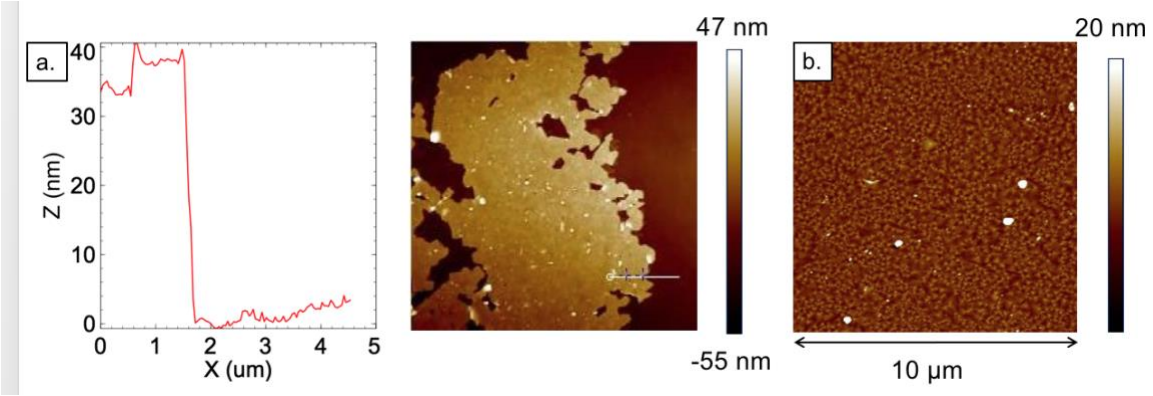

Figure 4.4: AFM of a.) step height of nominally 50nm transferred Bi flake and b.) surface morphology of 30nm transferred Bi film

Atomic force microscopy (AFM) has been used to measure the thickness of a delaminated Bi flake (Figure 4.4a). The measured step height of approximately 40nm is near the expected film thickness. This good accordance indicates that the entire film is being delaminated from the Si substrate as opposed to a single or few layers being exfoliated. This is a unique process which is dependent on both the interlayer bonding in the Bi films and the low adhesion of the film to its epitaxial substrate. Unfortunately, this indicates an inability to perform this kind of processing on bulk crystals as is possible with

the exfoliation of graphene. In addition, AFM measurements of transferred films (figure 4.4b) indicate that the planar nature of the films is retained in small areas of approximately 10 μm x 10 μm. The RMS roughness of a representative transferred film is found to be 1.14 nm, which is similar to the expected 1 nm RMS roughness of an as-grown 30 nm Bi film.

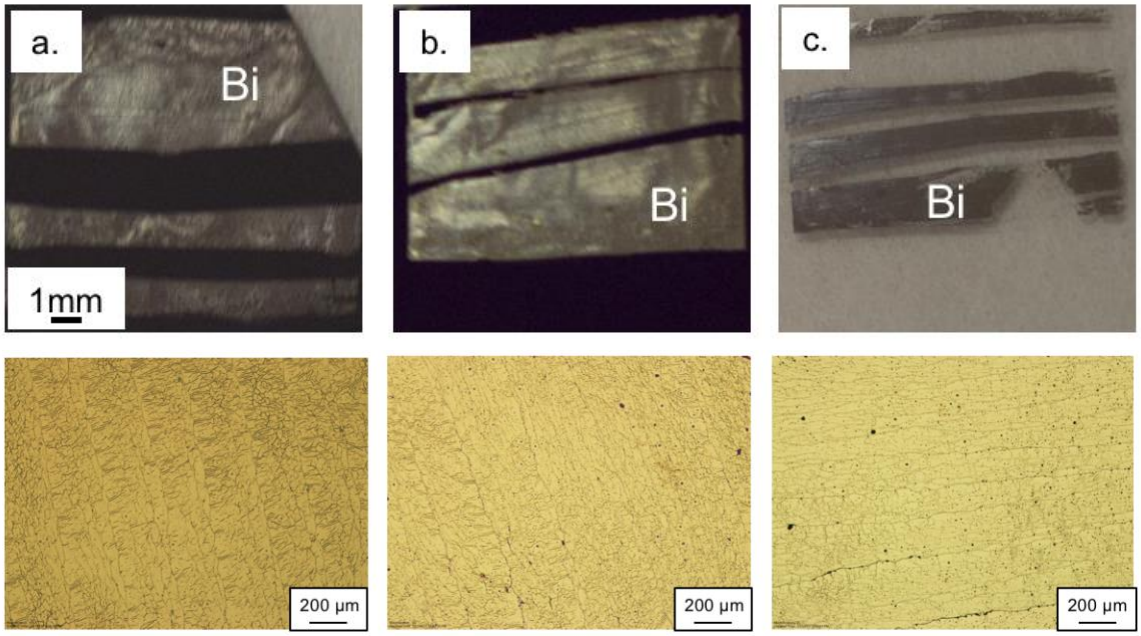

Figure 4.5: Transfer of 30nm Bi films to a.) Si, b.) SiO_2, c.) Glass

The similar transferred film area and quality on different transferred substrates is indicative that the transfer process is not dependent on bonding between the Bi film and the new substrate. Transfers have been successfully completed to handle substrates made of Si, SiO_2, glass, and yttrium iron garnet (YIG). Transfers on SiO_2 have potential for backgated electrical measurements which will allow exploration of the film properties a the Fermi level is shifted. Transfers on glass will allow measurements which require optically transparent substrates such as phonon dynamics measurements. Finally, transfers on YIG will allow spin-dependent measurements such as the integer spin Hall effect and spin-Seebeck measurements.

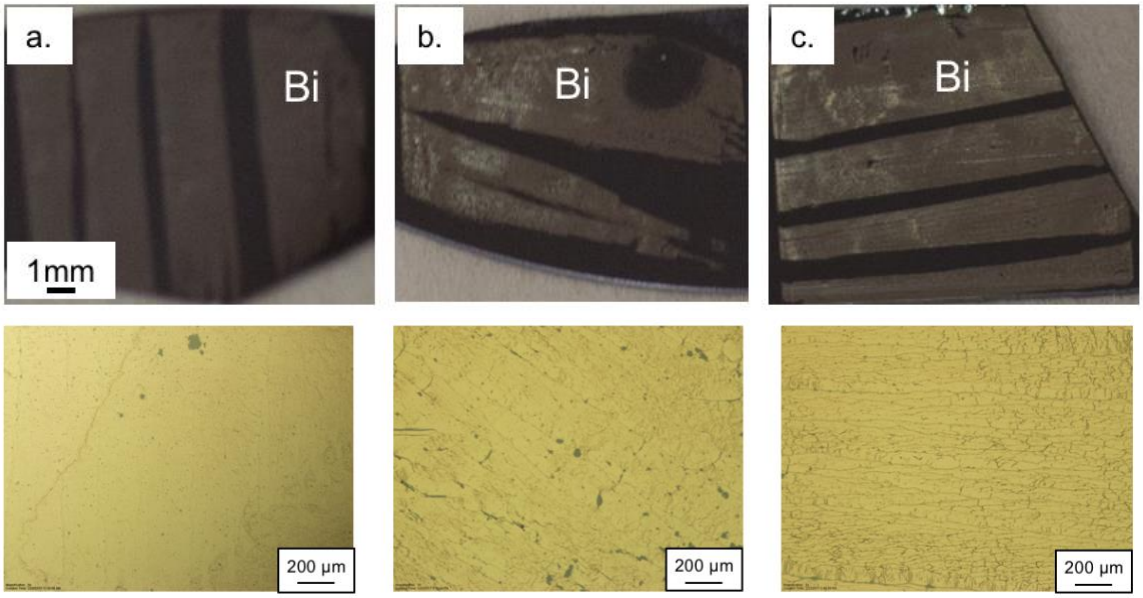

Figure 4.6: Transfer of a.) 20nm, b.) 30nm, and c.) 50nm Bi films to Si

We have found that we are unable to transfer films thinner than 20nm. As we have found no crystal structure transitions or changes in growth mode at this apparent critical thickness, the mechanism through which thinner films are unable to be transferred is likely related to surface effects such as oxidation or differences in surface roughness. The ability to achieve similarly large areas of film delamination at different film thicknesses (figure 4.7) above a critical thickness between 15 nm and 20 nm indicates that there is some unclear transition in the behavior of the adhesion of either the tape to the Bi or the Bi to the Si substrate. The apparent reduction in planarity and film quality in the thicker films might be attributed to the increased surface roughness as the film thickness increases.

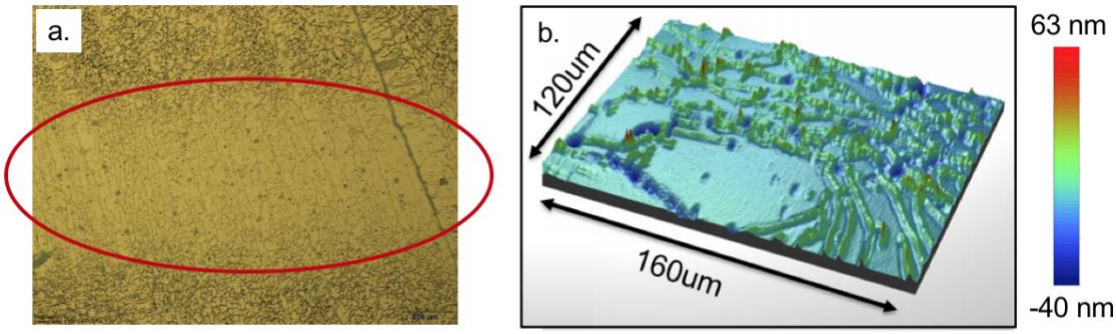

Figure 4.7: Demonstration of ripples in film using a.) optical microscopy and b.) optical profilometry

The presence of ripples in the transferred films have been ascertained using optical profilometry (Figure 4.7b). These ripples appear to be continuous areas of Bi and form at some point during the transfer process. These ripples likely originate due to the reduced strain experienced by the Bi film when they are removed from their epitaxial substrate. As the transferred Bi films do not appear to bond to their target substrate, the lattice will freely relax once it is no longer being held in its as-grown structure by the adhesion of the tape. This lack of bonding to the handle substrate indicates that the transferred films exhibit similar to a freestanding membrane. This is in contrast to the DCB transfers where the films remain bonded to the epoxy are limited in the amount they can relax.

Attempts at removing the ripples in the film by attempting to smooth the film before the tape is released has seen moderate success (Figure 4.7a). This is achieved through firmly pressing a flat instrument, such as flat-top tweezers, to the tape and sliding it across the surface of the tape. While this successfully makes the film more planar, this processing tends to create large discontinuities in the film if appropriate care is not taken. This also demonstrates that the ripples in the film are still continuous and are able to be removed or reduced through appropriate processing.

4.3.3 Electrical and Optical characterization of transferred films

Measurements of the film orientation as well as its electrical and optical qualities is performed on transferred samples to examine the robustness of these features to the transfer process.

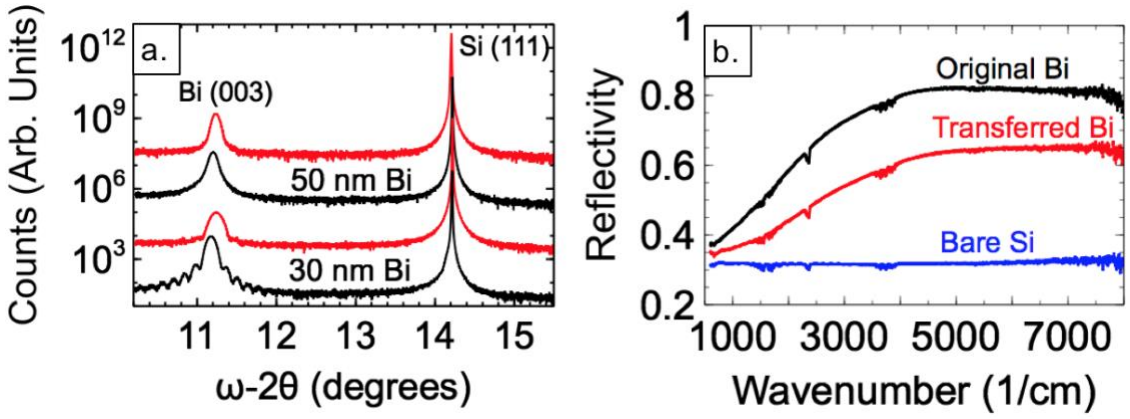

Figure 4.8: a.) XRD measurements and b.) Fourier Transform Infrared Spectroscopy (FTIR) measurements of as-grown (black) and transferred (red) films

XRD measurements of the Bi films before and after transfer indicate that the (001) orientation of the films is retained after transfer. The slight shift of the (001) peak is consistent with a shift of the in-plane lattice constant to that of bulk Bi. Interference fringes seen in the transferred films indicate that the transferred film remains single-crystalline and the interface between the Bi and the handle substrate is well-ordered. It is evident from the reflectivity spectrum (Figure 4.8b) that the reflectivity of the transferred films is reduced by approximately 25%, likely due to discontinuities and microcracking in the films. However, the reflectivity before and after transfer exhibits similar features (such as the drop-off around 4000 cm^{-1}) indicating preservation of the film's optical properties.

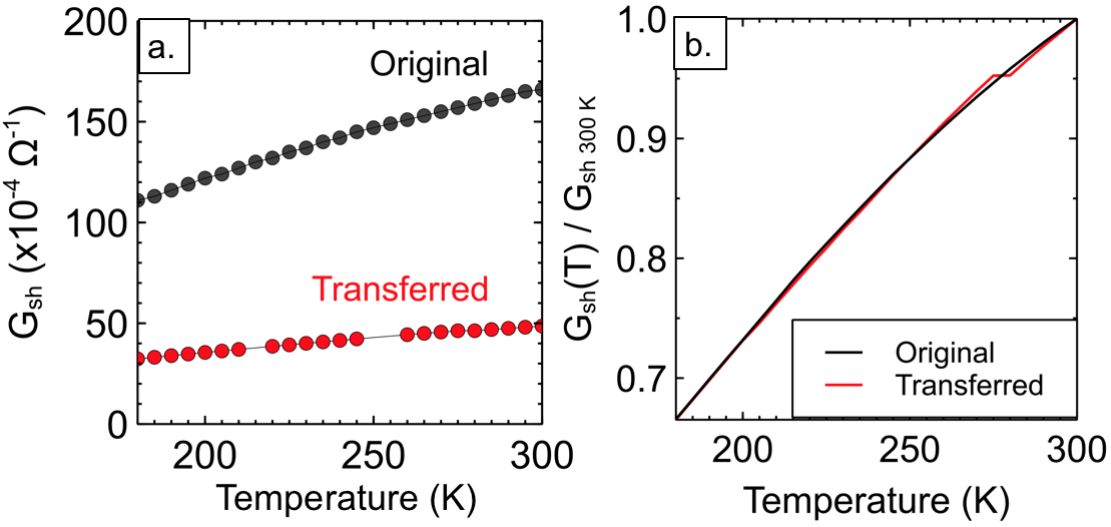

Figure 4.9: Temperature-dependent sheet conductance measurements of as grown and transferred Bi films a.) normalized to the value at 300K and b.) absolute sheet conductance measurements

Temperature-dependent sheet conductance measurements (Figure 4.9) before and after transfer indicate that the film's overall temperature-dependent transport behavior is retained although the overall sheet conductance is reduced. The reduction in sheet conductance is likely due to discontinuities in the film as the measurements are performed over films of fairly large areas on the order of 1 cm^2 . The conductance of the as-grown and transferred films normalized to 300K is extremely consistent, indicating the energy and nature of the quantum confined bandgap is robust to transfer. These measurements indicate that the unique electronic properties of Bi are retained through the transfer process and thus there is great potential to examine them on a wide variety of substrates with this method.

4.3.4 Transfer Optimization

Rreduction of discontinuities and ripples in the transferred films is necessary for large area measurements. We have attempted to improve transferred film quality through two primary avenues: release temperature and tape adhesion.

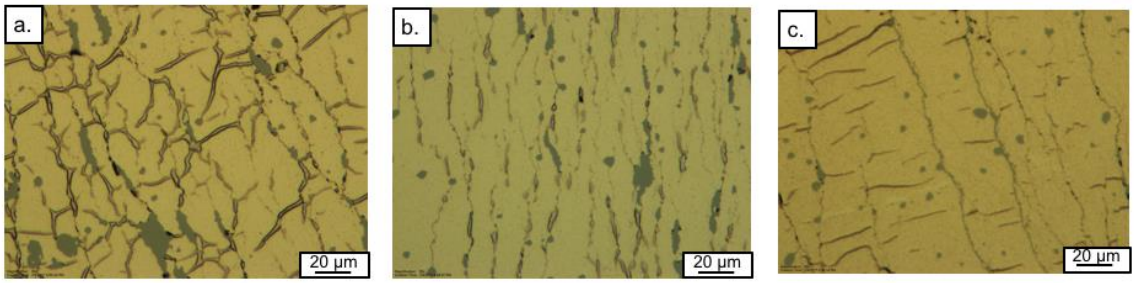

Figure 4.10: Transferred film quality at release temperatures a.) 120 °C, b.) 170 °C and c.) 210 °C

We have found that the use of a higher release temperature than that indicated by the manufacturer increases the continuity of the transferred films and reduces the density of ripples (Figure 4.10). The higher temperature may encourage faster expansion of the foam spheres such that the Bi does not experience as extended times of stress during the release. The higher temperature may also make it such that the foam spheres reach their transition temperature more uniformly due to the overshoot – resulting in the Bi film experiencing more uniform strain as the spheres expand.

The effect of a higher adhesion tape of 0.24 N/mm on transfer quality was tested on 30 nm Bi films (Figure 4.11). This tape was found to delaminate similar areas of Bi with potentially greater continuity, however, it left significantly more tape residue behind. Although a majority of tape residue has been found to be removable through solvent cleaning, the inability to use more aggressive, dry, cleanings on these films makes the increased quantity of residue undesirable.

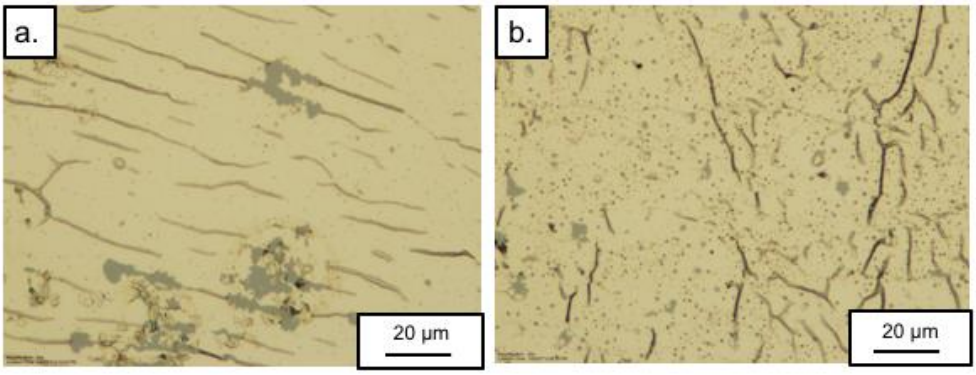

Figure 4.11: Transferred film quality using films with adhesions of a.) 0.185 N/mm, and b.) 0.24 N/mm

4.3.5 Origin of Weak Adhesion

The ability to easily delaminate Bi from its epitaxial substrate is surprising due to its covalent interlayer bonding as well as the typically high adhesion energy of epitaxially grown films. The measured adhesion energy of Bi on its epitaxial Si substrate is measured as 1 J/mm^2 which is more similar in magnitude to that of graphene (~-0.5 J/mm^2) than to other epitaxially grown materials such as GaAs (13 J/mm^2)[83]. This surprisingly low adhesion may be due to the unique growth modes present in the first few monolayers of Bi growth. It is well known that Bi initially forms a rugged wetting layer in its initial stages of growth[38], [84]. *In situ* XRD measurements have found that the interface spacings of the wetting layer are surprisingly large resulting in the nearly freestanding film behavior[85]. Previous studies of Bi films grown on Si (111) using ARPES have noted that the band structure closely resembles that of a freestanding Bi film with both surfaces having interfaces with vacuum[42]. The formation of the puckered layer allotrope in very thin films of Bi, and later allotropic transformation to the bulk rhombohedral structure, may also impact the interaction of the Bi film and the Si substrate, but ramifications of this transformation are thus far unknown. This is also good news that epitaxial films with

similar growth modes may also exhibit similarly weak adhesion and be accessible for mechanical transfer.

4.3.6 Transfer of $Bi_{1-x}Sb_x$

The similar crystal structure and RHEED patterning during growth of Bi and $Bi_{1-x}Sb_x$ is a good predictor that $Bi_{1-x}Sb_x$ may exhibit similarly weak bonding at the substrate interface. To our knowledge, no *in situ* studies of $Bi_{1-x}Sb_x$ have been performed to examine its structure at early stages of growth. However, theoretical predictions indicate that a puckered layer phase of $Bi_{1-x}Sb_x$ would be stable at monolayer thicknesses[86].

We have found that we are able to transfer both (001) and (012) oriented $Bi_{1-x}Sb_x$ indicating that both crystalline orientations exhibit weak adhesion to the growth substrate. No modifications to the thermal tape transfer method developed for Bi have been found to be necessary for large area transfers of $Bi_{1-x}Sb_x$. However, the continuity of the $Bi_{1-x}Sb_x$ transfers is seen to be reduced compared to similar thicknesses of transferred pure Bi films.

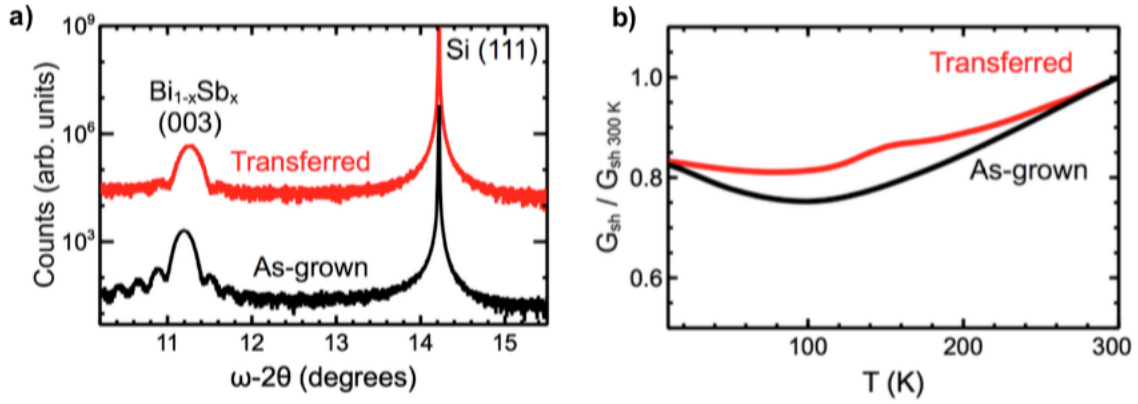

Figure 4.12: a.) XRD and b.) temperature dependent sheet conductance measurements of as-grown and transferred $Bi_{0.96}Sb_{0.04}$

XRD measurements of as-grown and transferred (001) $Bi_{0.96}Sb_{0.04}$ (figure 4.12a) indicate that the film retains its orientation through the transfer process, and the presence

of interference fringes indicate that the $Bi_{0.96}Sb_{0.04}$/Si interface is well ordered similar to the Bi case. Temperature dependent sheet conductance measurements of the as-grown and transferred films similarly shows that the electronic properties of the films are maintained through the transfer process. The irregular feature seen around 150K may be due to variation in the wire-bonded contact as the temperature changes. The increasing sheet conductance with temperature above 100K indicates that the semiconducting nature of the film is maintained. The decreasing sheet conductance with temperature below 100K is associated with the presence of metallic surface states in Bi, and which we have shown good indication are be present in (001) oriented $Bi_{0.96}Sb_{0.04}$ in Chapter 3 [64]. The apparent retention of these surface states is a good indication that they are robust to the transfer process in both (001) oriented $Bi_{0.96}Sb_{0.04}$ and pure Bi.

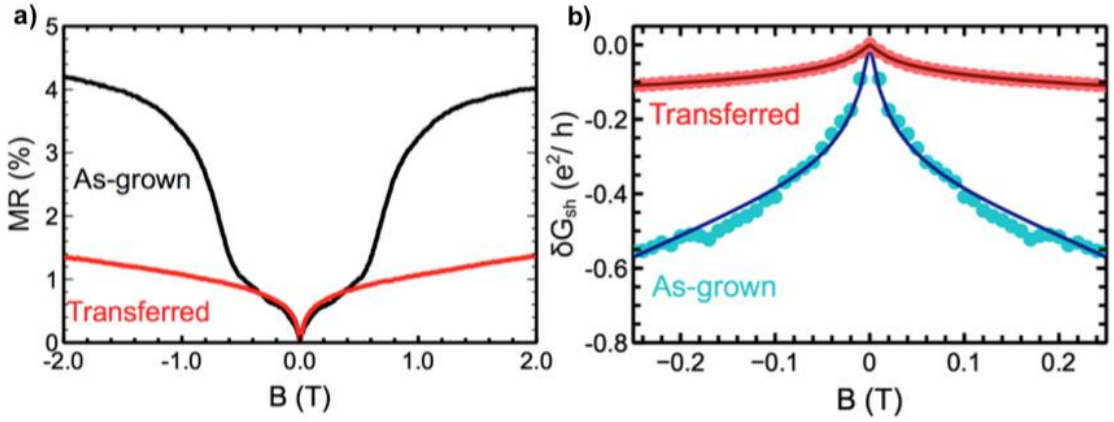

Figure 4.13: a.) Magnetoresistance measurements of transferred and as-grown $Bi_{0.96}Sb_{0.04}$ films and b.) Fitted low-field WAL feature

Low temperature magnetoresistance measurements of the $Bi_{0.96}Sb_{0.04}$ film indicate that both the as-grown and transferred sample exhibit the characteristic low-field cusp of WAL (Figure 4.13a). This feature can be fit to the HLN equation as discussion in chapter 3.8 (Figure 4.13b). The resulting fit finds an α parameter of 0.4 for the as-grown film which

matches with the expected values for a symplectic surface channel as seen in TIs as well as Bi films[63], [68]. Fitting the transferred film WAL feature results in a calculated α parameter of 0.1. This may indicate that the transfer process has caused an increase in the coupling of the surface channel to the bulk or introduced some other perturbation in the film. However, greater study is necessary to more conclusively identify the origin of this reduction in the α parameter.

Notably, the as-grown sample exhibits an additional dip in the MR at 1 T that is not present in the transferred film. This has not been previously reported to our knowledge and further measurements are necessary to identify its origin. One plausible explanation is that this feature arises from two surface channels contributing to transport, but only one experiencing coupling to the bulk[74]. This would also explain the non-quadratic behavior seen between the two dips around 0.2 T. However, each symplectic channel contributing to transport is expected to provide an additional factor of 0.5 to the α parameter, so the reported value is unexpectedly low for multi-channel behavior[76].

4.3.7 Epitaxial Bi as a Release Layer

Although $Bi_{1-x}Sb_x$ is able to be transferred using the same method as Bi, the transferred area and continuity is somewhat reduced (Figure 4.14a and b). Although this smaller area still retains the expected material properties of $Bi_{1-x}Sb_x$ films, the ability to transfer larger areas is appealing for the production of higher quality transferred films. We have found that the quality of transferred $Bi_{1-x}Sb_x$ can be significantly increased by the growth of a pure Bi release layer prior to the growth of the $Bi_{1-x}Sb_x$ film (Figure 4.14c). In addition, a five-layer heterostructure of alternating 10nm Bi and $Bi_{0.70}Sb_{0.30}$ layers was transferred using this method with similar success. The markedly improved quality seen

using this process implies that Bi has great potential as a release layer for other epitaxial films.

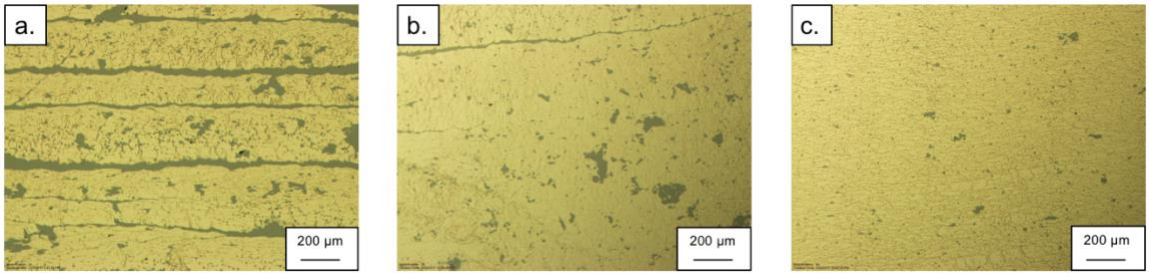

Figure 4.14: Transferred films of a.) 30nm $Bi_{0.75}Sb_{0.25}$ b.) 50nm $Bi_{0.75}Sb_{0.25}$, and c.) 20nm $Bi_{0.75}Sb_{0.25}$ on 30nm Bi

XRD measurements of the as-grown and transferred heterostructures were performed to confirm that the crystal structure was maintained through this processing (Figure 4.15). As with the Bi and $Bi_{1-x}Sb_x$ films, these measurements indicate that the crystal structure is robust to transfer. In addition, we note that orientation of both films is in the (001) direction although we would expect high Sb composition films such as these to be (012) oriented. This implies that the growth of (001) oriented high Sb concentration $Bi_{1-x}Sb_x$ films is possible with the use of a Bi buffer layer. This result could allow the measurement of quantum confined (001) oriented $Bi_{1-x}Sb_x$ across a much larger range of Sb concentrations, allowing the direct comparison of bulk topologically insulating $Bi_{1-x}Sb_x$ and quantum confined topologically insulating $Bi_{1-x}Sb_x$.

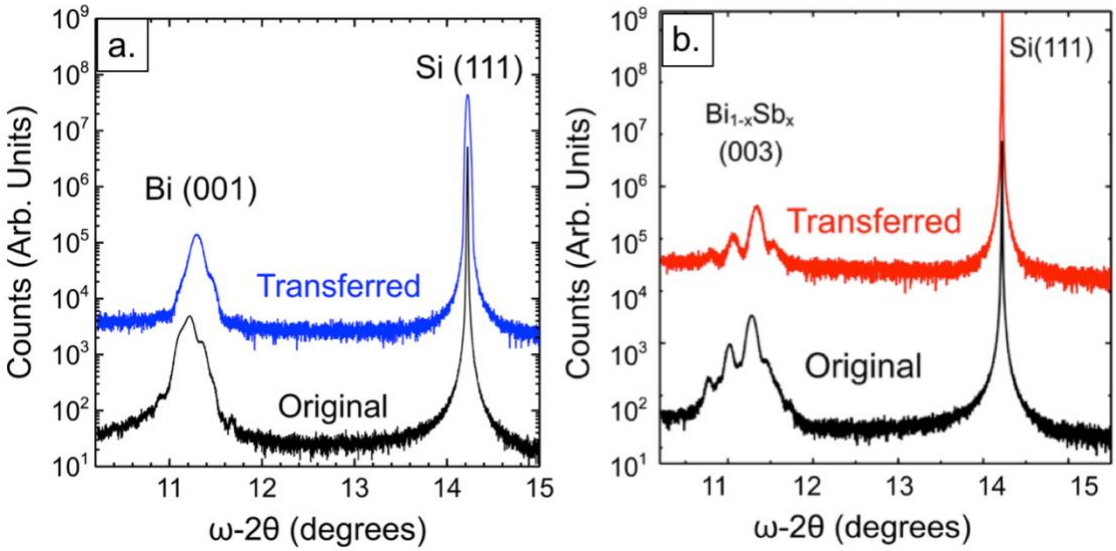

Figure 4.15: XRD of as-grown and transferred a.) 20nm $Bi_{0.75}Sb_{0.25}$ on 30nm Bi and b.) five-layer alternating $Bi_{0.70}Sb_{0.30}$ / Bi heterostructure

Chapter 5: Conclusions

In this work, we have explored the role of quantum confinement in the properties of highly crystalline epitaxial Bi and $Bi_{1-x}Sb_x$ thin films. We have defined the boundaries of thickness regimes where Bi experiences unique transport phenomena. We have also identified a new crystal structure of $Bi_{1-x}Sb_x$ that is (012) oriented and dependent on alloy composition. We have found that the (012) oriented $Bi_{1-x}Sb_x$ films exhibit fundamentally different electronic properties when probed using temperature-dependent sheet conductance measurements. We have also identified the number and nature of transport channels contributing to the electronic properties seen in Bi using variable magnetic field Hall measurements and MR measurements. We have shown that Bi exhibits a WAL feature at low fields as expected for its large spin-orbit interaction and discussed the likely transport contributions to its low field behavior. We have also observed higher field dips in Bi's MR that have not been previously reported to our knowledge and may indicate unique properties of the transport in quantum confined Bi.

In addition, we have demonstrated that both epitaxial Bi and $Bi_{1-x}Sb_x$ are very weakly interacting with the Si (111) substrates on which they are grown, which facilitates the simple dry transfer of these films. We have found that these dry transfer methods allow the transfer of both Bi and $Bi_{1-x}Sb_x$ to arbitrary substrates. These transferred areas are found to retain their crystal structure and transport phenomena.

Our recommendations for future work on this materials system comes in three thrusts: gated measurements to better distinguish between bulk and surface contributions to the transport, measurements of spin-based phenomena to quantify the mechanisms through which these films would be useful for spintronic devices, and *in situ* studies using ARPES and STM to confirm predicted properties of these films. The developed dry transfer

methods may facilitate the performance of these measurements by allowing the transfer of high quality epitaxial films to insulating and magnetic substrates. This would be useful for the performance of gated and spin-transport measurements. In addition, a modified transfer method may facilitate the *in situ* delamination of these films. Performing studies of these metrics would help unravel unanswered questions about the nature of quantum confined single-crystalline Bi and $Bi_{1-x}Sb_x$ films and would promote the early stages of development of devices based on these materials' spin properties.

References

[1] I. Zutic, J. Fabian, and S. Das Sarma, "Spintronics : Fundamentals and applications," *Rev. Mod. Phys.*, vol. 76, pp. 323–386, 2004.

[2] D. D. Awschalom, L. C. Bassett, A. S. Dzurak, E. L. Hu, and J. R. Petta, "Quantum spintronics: Engineering and manipulating atom-like spins in semiconductors," *Science (80-.).*, vol. 339, no. 6124, pp. 1174–1179, 2013.

[3] K. D. Petersson *et al.*, "Circuit quantum electrodynamics with a spin qubit," *Nature*, vol. 490, no. 7420, pp. 380–383, 2012.

[4] T. Hirahara *et al.*, "Direct observation of spin splitting in bismuth surface states," *Phys. Rev. B*, vol. 76, pp. 153305-1-153305–4, 2007.

[5] D. Hsieh *et al.*, "A topological Dirac insulator in a quantum spin Hall phase," *Nature*, vol. 452, pp. 970–975, 2008.

[6] T. Nagao, T. Doi, T. Sekiguchi, and S. Hasegawa, "Epitaxial Growth of Single-Crystal Ultrathin Films of Bismuth on Si (111)," *Jpn. J. Appl. Phys.*, vol. 39, pp. 4567–4570, 2000.

[7] A. D. Kent and D. C. Worledge, "A new spin on magnetic memories," *Nat. Nanotechnol.*, vol. 10, no. 3, pp. 187–191, 2015.

[8] D. C. Ralph and M. D. Stiles, "Spin transfer torques," *J. Magn. Magn. Mater.*, vol. 320, no. 7, pp. 1190–1216, 2008.

[9] K. L. Wang, J. G. Alzate, and P. Khalili Amiri, "Low-power non-volatile spintronic memory: STT-RAM and beyond," *J. Phys. D. Appl. Phys.*, vol. 46, no. 8, 2013.

[10] P. Gambardella and I. M. Miron, "Current-induced spin-orbit torques," *Philos. Trans. R. Soc. A Math. Phys. Eng. Sci.*, vol. 369, no. 1948, pp. 3175–3197, 2011.

[11] M. Yang, K. Cai, H. Ju, K. W. Edmonds, G. Yang, and S. Liu, "Spin-orbit torque in Pt / CoNiCo / Pt symmetric devices," *Nat. Publ. Gr.*, no. October 2015, pp. 1–7, 2016.

[12] M. I. Dyakonov and V. I. Perel, "Current-induced spin orientation of electrons in semiconductors," *Phys. Lett. A*, vol. 35, no. 6, pp. 459–460, 1971.

[13] D. Pesin and A. H. MacDonald, "Spintronics and pseudospintronics in graphene and topological insulators," *Nat. Mater.*, vol. 11, no. 5, pp. 409–416, 2012.

[14] L. Liu, A. Richardella, I. Garate, Y. Zhu, N. Samarth, and C.-T. Chen, "Spin-Polarized Tunneling Study on Spin-Momentum Locking in Topological Insulators," *Phys. Rev. B*, vol. 91, p. 235437, 2015.

[15] A. R. Mellnik *et al.*, "Spin-transfer torque generated by a topological insulator," *Nature*, vol. 511, no. 7510, pp. 449–451, 2014.

[16] C. L. Kane, *Topological Insulators*, Volume 6. Elsevier, 2013.

[17] K. V Klitzing, G. Dorda, and M. Pepper, "A New Method for High-Accuracy Determination of th Fine-Structure Constant Based on Quantized Hall Resistance," *Phys. Rev. Lett.*, vol. 45, no. 6, pp. 494–497, 1980.

[18] B. A. Bernevig, T. L. Hughes, and S. Zhang, "Quantum Spin Hall Effect and Topological Phase Transition in Hgte Quantum Wells," *Science (80-.).*, vol. 314,

no. 5806, pp. 1757–1761, 2006.
[19] C. L. Kane and E. J. Mele, “Z2 topological order and the quantum spin hall effect,” *Phys. Rev. Lett.*, vol. 95, no. 14, pp. 3–6, 2005.
[20] L. Fu, C. L. Kane, and E. J. Mele, “Topological Insulators in Three Dimensions,” no. 1, pp. 2–5, 2006.
[21] M. Kohmoto, B. I. Halperin, and Y. Wu, “Diophantine equation for the three-dimensional quantum Hall effect,” *Phys. Rev. B*, vol. 45, no. 23, pp. 488–493, 1992.
[22] L. Fu and C. L. Kane, “Topological Insulators with Inversion Symmetry,” *Phys. Rev. B*, vol. 76, no. 4, p. 45302, 2007.
[23] M. König *et al.*, “Quantum Spin Hall Insulator in HgTe Quantum Wells State,” *Science (80-.).*, vol. 318, no. 5851, pp. 766–770, 2007.
[24] K. C. Hasan, M Z, “Colloquium : Topological insulators,” *Rev. Mod. Phys.*, vol. 82, pp. 3045–3067, 2010.
[25] L. Fu and C. L. Kane, “Superconducting proximity effect and Majorana fermions at the surface of a topological insulator,” no. 3, pp. 1–4, 2007.
[26] F. Nakamura *et al.*, “Topological transition in Bi 1-xSb x studied as a function of Sb doping,” *Phys. Rev. B - Condens. Matter Mater. Phys.*, vol. 84, no. 23, pp. 1–8, 2011.
[27] T. Trivedi, S. Sonde, H. C. P. Movva, and S. K. Banerjee, “Weak antilocalization and universal conductance fluctuations in bismuth telluro-sulfide topological insulators,” *J. Appl. Phys.*, vol. 119, no. 5, 2016.
[28] N. Bansal *et al.*, “Epitaxial growth of topological insulator Bi2Se3 film on Si(111) with atomically sharp interface,” *Thin Solid Films*, vol. 520, pp. 224–229, 2011.
[29] H. Zhang, C.-X. Liu, X.-L. Qi, X. Dai, Z. Fang, and S.-C. Zhang, “Topological insulators in Bi2Se3, Bi2Te3 and Sb2Te3 with a single Dirac cone on the surface,” *Nat. Phys.*, vol. 5, no. 6, pp. 438–442, 2009.
[30] N. H. Duy Khang, Y. Ueda, K. Yao, and P. N. Hai, “Growth and characterization of MnGa thin films with perpendicular magnetic anisotropy on BiSb topological insulator,” *J. Appl. Phys.*, vol. 122, p. 143903, 2017.
[31] E. I. Rogacheva *et al.*, “Quantum-size effects in n-type bismuth thin films,” *Appl. Phys. Lett.*, vol. 82, no. 16, pp. 2628–2630, 2003.
[32] T. Hirahara, “The Rashba and quantum size effects in ultrathin Bi films,” *J. Electron Spectros. Relat. Phenomena*, vol. 201, pp. 98–104, 2015.
[33] T. Hirahara *et al.*, “Role of Quantum and Surface-State Effects in the Bulk Fermi-Level Position of Ultrathin Bi Films,” *Phys. Rev. Lett.*, vol. 115, pp. 106803-1-106803–5, 2015.
[34] V. B. Sandomirskii, “Quantum Size Effect in a Semimetal Film,” *Sov. Phys. JETP*, vol. 25, no. 1, 1967.
[35] Y. F. Ogrin, V. N. Lutskii, M. U. Arifova, V. I. Kovalev, V. B. Sandomirskii, and M. I. Elinson, “Temperature Dependence of the Resistivity and of the Hall Coefficient of Size-Quantized Bismuth Films,” *Sov. Phys. JETP*, vol. 26, no. 4, pp. 714–717, 1968.

[36] N. Marcano *et al.*, "Role of the surface states in the magnetotransport properties of ultrathin bismuth films," *Phys. Rev. B*, vol. 82, no. 12, p. 125326, Sep. 2010.
[37] T. Hirahara *et al.*, "Role of Spin-Orbit Coupling and Hybridization Effects in the Electronic Structure of Ultrathin Bi Films," *Phys. Rev. Lett.*, vol. 97, pp. 146803-1-146803–4, 2006.
[38] J. T. Sadowski *et al.*, "Thin bismuth film as a template for pentacene growth," *Appl. Phys. Lett.*, vol. 86, no. 7, pp. 1–3, 2005.
[39] S. Yaginuma and T. Nagao, "Origin of flat morphology and high crystallinity of ultrathin bismuth films," *Surf. Sci.*, vol. 601, pp. 3593–3600, 2007.
[40] T. Nagao *et al.*, "Nanofilm Allotrope and Phase Transformation of Ultrathin Bi Film on Si(111)-7×7," *Phys. Rev. Lett.*, vol. 93, no. 10, p. 105501, Aug. 2004.
[41] E. Aktürk, O. Ü. Aktürk, and S. Ciraci, "Single and bilayer bismuthene: Stability at high temperature and mechanical and electronic properties," *Phys. Rev. B - Condens. Matter Mater. Phys.*, vol. 94, no. 1, pp. 1–9, 2016.
[42] T. Hirahara *et al.*, "Quantum well states in ultrathin Bi films: Angle-resolved photoemission spectroscopy and first-principles calculations study," *Phys. Rev. B - Condens. Matter Mater. Phys.*, vol. 75, no. 3, pp. 1–9, 2007.
[43] S. C. S. Cho, Y. K. Y. Kim, a. DiVenere, G. K. Wong, J. B. Ketterson, and J. R. Meyer, "Anisotropic Seebeck and magneto-Seebeck coefficients of Bi and BiSballoy thin films," *Eighteenth Int. Conf. Thermoelectr. Proceedings, ICT'99 (Cat. No.99TH8407)*, vol. 808, no. 2000, pp. 1–6, 1999.
[44] G. E. Smith and R. Wolfe, "Thermoelectric Properties of Bismuth-Antimony Alloys," *J. Appl. Phys.*, vol. 33, no. 3, p. 841, 1962.
[45] D. Hsieh *et al.*, "Observation of topologically protected Dirac spin-textures and π Berry's phase in pure Antimony (Sb) and topological insulator BiSb," vol. 919, pp. 1–10, 2009.
[46] M. Y. Tang and M. S. Dresselhaus, "A Band Structure Phase Diagram Calculation of 2D BiSb Films," *Mater. Res. Soc. Symp. Proc. Vol.*, vol. 886, pp. 1–6, 2006.
[47] Y. M. Koroteev *et al.*, "Strong Spin-Orbit Splitting on Bi Surfaces," *Phys. Rev. Lett.*, vol. 93, no. 4, pp. 46403-1-46403–4, 2004.
[48] S. Tang and M. S. Dresselhaus, "Phase Diagrams of Bi1−xSbx Thin Films with Different Growth Orientations," *Phys. Rev. B*, vol. 86, p. 75436, 2012.
[49] T. Hirahara *et al.*, "Topological metal at the surface of an ultrathin Bi 1 − x Sb x alloy film," *Phys. Rev. B*, vol. 81, p. 165422, 2010.
[50] S. Cho *et al.*, "Molecular beam epitaxial growth and structural properties of Bi 1 − x Sb x alloy thin films on CdTe (111) substrates Molecular beam epitaxial growth and structural properties of Bi 1 ⁻ x Sb x alloy thin films on CdTe „ 111 … substrates," *J. Vac. Sci. Technol. A*, vol. 17, no. 1, pp. 9–13, 1999.
[51] D. T. Morelli, D. L. Partin, and J. Heremans, "Galvanomagnetic properties of single-crystal bismuth-antimony thin films," *Semicond. Sci. Technol.*, vol. 5, pp. S257–S259, 1990.
[52] Y. Ueda, N. H. Duy Khang, K. Yao, and P. N. Hai, "Epitaxial growth and characterization of Bi1-xSbx spin Hall thin films on GaAs(111)A substrates,"

Appl. Phys. Lett., vol. 110, no. 6, p. 62401, 2017.
[53] E. S. Walker, "Phase Transitions , Transfer and Nanoscale Growth of Epitaxial Bi and Bi 1-x Sb x Thin Films," 2018.
[54] T. Nagao *et al.*, "Nanofilm Allotrope and Phase Transformation of Ultrathin Bi Film on Si (111) - 7 x 7," *Phys. Rev. Lett.*, vol. 93, no. 10, pp. 105501-1-105501–4, 2004.
[55] L. A. Falkovskii, "Physical properties of bismuth," *Sov. Phys. Uspekhi*, vol. 11, no. 1, pp. 1–21, 1968.
[56] T. Hirahara, I. Matsuda, S. Yamazaki, N. Miyata, and S. H. Nagao, "Large surface-state conductivity in ultrathin Bi films," *Appl. Phys. Lett.*, vol. 91, pp. 202106-1-202106–3, 2007.
[57] D. K. Schroder, *Semiconductor Material and Device Characterization*. 2006.
[58] R. A. Hoffman and D. R. Frankl, "Electrical Transport Properties of Thin Bismuth Films," vol. 552, 1970.
[59] D. L. Partin, J. Heremans, D. T. Morelli, C. M. Thrush, C. H. Olk, and T. A. Perry, "Growth and Characterization of Epitaxial Bismuth Films," *Phys. Rev. B*, vol. 38, no. 6, pp. 3818–3825, 1988.
[60] N. Marcano *et al.*, "Role of the surface states in the magnetotransport properties of ultrathin bismuth films," *Phys. Rev. B*, vol. 82, pp. 125326-1-125326–6, 2010.
[61] D. Lükermann, S. Sologub, H. Pfnür, and C. Tegenkamp, "Sensing surface states of Bi films by magnetotransport," *Phys. Rev. B*, vol. 83, pp. 1–5, 2011.
[62] H. Wang *et al.*, "Crossover between weak antilocalization and weak localization of bulk states in ultrathin Bi2Se3 films," *Sci. Rep.*, vol. 4, pp. 1–23, 2014.
[63] M. Aitani, T. Hirahara, S. Ichinokura, M. Hanaduka, D. Shin, and S. Hasegawa, "*In situ* Magnetotransport Measurements in Ultrathin Bi Films: Evidence for Surface-Bulk Coherent Transport," *Phys. Rev. Lett.*, vol. 113, no. 20, p. 206802, Nov. 2014.
[64] S. Xiao, D. Wei, and X. Jin, "Bi (111) Thin Film with Insulating Interior but Metallic Surfaces," *Phys. Rev. B*, vol. 109, pp. 166805-1-166805–5, 2012.
[65] I. Matsuda *et al.*, "Electron-phonon interaction and localization of surface-state carriers in a metallic monolayer," *Phys. Rev. Lett.*, vol. 99, no. 14, p. 146805, 2007.
[66] B. L. Altshuler, D. Khmel'nitzkii, A. I. Larkin, and P. A. Lee, "Magnetoresistance and Hall effect in a disordered two-dimensional electron gas," *Phys. Rev. B*, vol. 22, no. 11, pp. 5142–5153, 1980.
[67] G. Bergmann, "Influence of Spin-Orbit Coupling on Weak Localization," *Phys. Rev. Lett.*, vol. 48, no. 15, pp. 1046–1049, 1982.
[68] H. He, G. Wang, T. Zhang, I. Sou, G. K. L. Wong, and J. Wang, "Impurity Effect on Weak Antilocalization in the Topological Insulator Bi 2 Te 3," *Phys. Rev. Lett.*, vol. 2016, p. 166805, 2011.
[69] S. V Iordanskii, Y. B. Lyanda-Geller, and G. E. Pikus, "Weak Localization in Quantum Wells with Spin-Orbit Interaction," *JETP Lett.*, vol. 60, no. 3, pp. 206–211, 1994.

[70] L. E. Golub, I. V Gornyi, and V. Y. Kachorovskii, “Weak antilocalization in two-dimensional systems with large Rashba splitting,” *Phys. Rev. B*, vol. 93, p. 2453006, 2016.
[71] G. Tkachov, *Topological Insulators : The Physics of Spin Helicity in Quantum Transport*. Stanford Publishing, 2015.
[72] S. Hikami, A. I. Larkin, and Y. Nagaoka, “Spin-Orbit Interaction and Magnetoresistance in the Two Dimensional Random System,” *Prog. Theor. Phys.*, vol. 63, no. 2, pp. 707–710, 1980.
[73] K. Zhu *et al.*, “The emergence of topologically protected surface states in epitaxial Bi(111) thin films,” *arXiv Prepr. arXiv1403.0066*, 2014.
[74] H. Steinberg, J. B. Laloë, V. Fatemi, J. S. Moodera, and P. Jarillo-Herrero, “Electrically tunable surface-to-bulk coherent coupling in topological insulator thin films,” *Phys. Rev. B - Condens. Matter Mater. Phys.*, vol. 84, no. 23, pp. 5–8, 2011.
[75] J. Chen *et al.*, “Tunable surface conductivity in Bi2Se3 revealed in diffusive electron transport,” *Phys. Rev. B - Condens. Matter Mater. Phys.*, vol. 83, no. 24, pp. 1–4, 2011.
[76] F. Yang *et al.*, “Top gating of epitaxial $(Bi_{1-x}Sb_x)_2Te_3$ topological insulator thin films,” *Appl. Phys. Lett.*, vol. 104, no. 16, p. 161614, 2014.
[77] D. Kim, P. Syers, N. P. Butch, J. Paglione, and M. S. Fuhrer, “Coherent topological transport on the surface of Bi2Se3,” *Nat. Commun.*, vol. 4, no. May, pp. 1–5, 2013.
[78] E. S. Walker *et al.*, “Large-Area Dry Transfer of Single-Crystalline Epitaxial Bismuth Thin Films,” *Nano Lett.*, vol. 16, 2016.
[79] S. R. Na *et al.*, “Selective Mechanical Transfer of Graphene from Seed Copper Foil Using Rate Effects.,” *ACS Nano*, vol. 9, no. 2, pp. 1325–1335, 2015.
[80] S. R. Na *et al.*, “Clean graphene interfaces by selective dry transfer for large area silicon integration.,” *Nanoscale*, vol. 8, no. 14, pp. 7523–33, 2016.
[81] J. D. Caldwell *et al.*, “Techniques for the Dry Transfer of Epitaxial Graphene onto Arbitrary Substrates,” *Electrochem. Soc. Trans.*, vol. 33, no. 4, pp. 177–186, 2010.
[82] N. Corporation, “Thermal Release Sheet ‘REVALPHA.’” pp. 1–18, 2016.
[83] Z. Zong *et al.*, “Direct measurement of graphene adhesion on silicon surface by intercalation of nanoparticles Direct measurement of graphene adhesion on silicon surface by intercalation of nanoparticles,” *J. Appl. Phys.*, vol. 107, pp. 26104-1-26104–3, 2010.
[84] T. Nagao, T. Doi, T. Sekiguchi, and S. Hasegawa, “Epitaxial Growth of Single-Crystal Ultrathin Films of Bismuth on Si (111),” *Jpn. J. Appl. Phys.*, vol. 39, no. 111, pp. 4567–4570, 2000.
[85] T. Shirasawa, M. Ohyama, W. Voegeli, and T. Takahashi, “Interface of a Bi (001) film on Si (111) -7 × 7 imaged by surface x-ray diffraction,” *Phys. Rev. B*, vol. 84, p. 75411, 2011.
[86] C. G. Tan, P. Zhou, J. G. Lin, and L. Z. Sun, “Prediction of two-dimensional BiSb with puckered structure,” *Phys. Status Solidi RRL*, vol. 1700051, 2017.